AD________________

Award Number DAMD17-94-J-4055

TITLE: Direct Digital Mammography Using Capillary Optics

PRINCIPAL INVESTIGATOR: Carolyn A. MacDonald, Ph.D.

CONTRACTING ORGANIZATION: New York State University at Albany
Albany, New York 12222

REPORT DATE: July 1999

TYPE OF REPORT: Final

PREPARED FOR: U.S. Army Medical Research and Materiel Command
Fort Detrick, Maryland 21702-5012

DISTRIBUTION STATEMENT: Approved for Public Release;
Distribution Unlimited

The views, opinions and/or findings contained in this report are those of the author(s) and should not be construed as an official Department of the Army position, policy or decision unless so designated by other documentation.

DTIC QUALITY INSPECTED 4

20001013 115

REPORT DOCUMENTATION PAGE	*Form Approved* *OMB No. 0704-0188*

Public reporting burden for this collection of information is estimated to average 1 hour per response, including the time for reviewing instructions, searching existing data sources, gathering and maintaining the data needed, and completing and reviewing the collection of information. Send comments regarding this burden estimate or any other aspect of this collection of information, including suggestions for reducing this burden, to Washington Headquarters Services, Directorate for Information Operations and Reports, 1215 Jefferson Davis Highway, Suite 1204, Arlington, VA 22202-4302, and to the Office of Management and Budget, Paperwork Reduction Project (0704-0188), Washington, DC 20503.

1. AGENCY USE ONLY *(Leave blank)*	2. REPORT DATE July 1999	3. REPORT TYPE AND DATES COVERED Final (1 Sep 94 - 30 Jun 99)

4. TITLE AND SUBTITLE Direct Digital Mammography Using Capillary Optics	5. FUNDING NUMBERS DAMD17-94-J-4055
6. AUTHOR(S) Carolyn A. MacDonald, Ph.D.	
7. PERFORMING ORGANIZATION NAME(S) AND ADDRESS(ES) New York State University at Albany Albany, New York 12222	8. PERFORMING ORGANIZATION REPORT NUMBER
9. SPONSORING / MONITORING AGENCY NAME(S) AND ADDRESS(ES) U.S. Army Medical Research and Materiel Command Fort Detrick, Maryland 21702-5012	10. SPONSORING / MONITORING AGENCY REPORT NUMBER
11. SUPPLEMENTARY NOTES	
12a. DISTRIBUTION / AVAILABILITY STATEMENT Approved for Public Release; Distribution Unlimited	12b. DISTRIBUTION CODE

13. ABSTRACT *(Maximum 200 words)*

The overall objective of this proposal is to develop a mammographic system with extremely high scatter rejection and dynamic range, good resolution and low patient dose. This will be accomplished by developing a direct x-ray detector interfaced with a capillary x-ray optic. Capillary x-ray optics, invented in the mid-eighties, provide an innovative new way to control x-ray beams. A number of promising geometries are being studied: collimating optics with long and short focal lengths, with and without antiscatter optics, monolithic linear magnifying tapers, and monolithic focusing, demagnifying optics. The collimating optics have transmissions in excess of 30% at their design energies, with collection angles ranging from 8 to 12 degrees. Scatter rejection is very high from all the optics. The linear tapers resulted in nearly ideal contrast enhancements and simultaneously increase in MTF at all spatial frequencies. The rapidly growing modeling capability has lead to improvements in the manufacturing processes. Direct digital detectors owe their high efficiency and resolution to the direct detection of x-ray photons without requiring phosphors for the conversion to visible light. One dimensional "imaging" was demonstrated with the CZT linear array. CID two-dimensional arrays with small pixel sizes are another promising new technology for mammography.

14. SUBJECT TERMS Breast Cancer	15. NUMBER OF PAGES 64
	16. PRICE CODE

17. SECURITY CLASSIFICATION OF REPORT Unclassified	18. SECURITY CLASSIFICATION OF THIS PAGE Unclassified	19. SECURITY CLASSIFICATION OF ABSTRACT Unclassified	20. LIMITATION OF ABSTRACT Unlimited

FOREWORD

Opinions, interpretations, conclusions and recommendations are those of the author and are not necessarily endorsed by the U.S. Army.

CAM Where copyrighted material is quoted, permission has been obtained to use such material.

CAM Where material from documents designated for limited distribution is quoted, permission has been obtained to use the material.

CAM Citations of commercial organizations and trade names in this report do not constitute an official Department of Army endorsement or approval of the products or services of these organizations.

____ In conducting research using animals, the investigator(s) adhered to the "Guide for the Care and Use of Laboratory Animals," prepared by the Committee on Care and use of Laboratory Animals of the Institute of Laboratory Resources, national Research Council (NIH Publication No. 86-23, Revised 1985).

____ For the protection of human subjects, the investigator(s) adhered to policies of applicable Federal Law 45 CFR 46.

____ In conducting research utilizing recombinant DNA technology, the investigator(s) adhered to current guidelines promulgated by the National Institutes of Health.

____ In the conduct of research utilizing recombinant DNA, the investigator(s) adhered to the NIH Guidelines for Research Involving Recombinant DNA Molecules.

____ In the conduct of research involving hazardous organisms, the investigator(s) adhered to the CDC-NIH Guide for Biosafety in Microbiological and Biomedical Laboratories.

Carolyn MacDonald 9/17/99

PI - Signature Date

4. Table of Contents

1. Front Cover 1
2. Report Documentation 2
3. Foreword 3
4. Table of Contents 4
5. Introduction 6
  5.1. Nature of the Problem 6
  5.2. Purpose 6
6. Body 7
  6.1. Background 7
    6.1.1. Benefits of Digital Mammography 7
    6.1.2. Capillary Optics 7
    6.1.3. Digital X-ray Detection 8
  6.2. Proposed Statement of Work: Final Assessment 9
  6.3. Research Accomplishments 10
    6.3.1. Polycapillary Optics 10
      6.3.1.1. Single Fibers 10
        6.3.1.1.1. Transmission 10
        6.3.1.1.2. Absorption Measurements 18
      6.3.1.2. Collimating Optics 20
        6.3.1.2.1. 8 keV Prototype 20
          6.3.1.2.1.1. Transmission and Uniformity 20
        6.3.1.2.2. Divergence and Diffraction Gain 23
        6.3.1.2.3. 20 KeV prototypes 26
          6.3.1.2.3.1. 1 m focal length optic 26
          6.3.1.2.3.2. 2 m focal length optic 27
          6.3.1.2.3.3. 24 cm focal length optic 27
      6.3.1.3. Anti-Scatter Optics 27
        6.3.1.3.1. Straight MultiFiber Optic 27
        6.3.1.3.2. Magnifying Linear Monolithic Optics 28
          6.3.1.3.2.1. Transmission 28
          6.3.1.3.2.2. Defect Study 30
          6.3.1.3.2.3. Simulations 31
          6.3.1.3.2.4. Potential for Lead Glass 32
            6.3.1.3.2.4.1. Calculation of Contrast Improvement and Relative SNR ... 33
            Performance of Three Hypothetical Lenses 35
          6.3.1.3.2.5. Manufacturing Issues 36
          6.3.1.3.2.6. Imaging Measurements 41
        6.3.1.3.3. Multitaper Optic 42
      6.3.1.4. Artifact Reduction 43
      6.3.1.5. Demagnifying, Focusing Monolithic Optics 46
    6.3.2. Direct Digital Detectors 47
      6.3.2.1. CZT Detector 47
          6.3.2.1.1.1. Single pixel CZT detector 48
          6.3.2.1.1.2. Linear array 50

        - 6.3.2.2. CID Detectors 52
- 7. Key Research Accomplishments 53
- 8. Reportable Outcomes 53
  - 8.1. Manuscripts 53
  - 8.2. Presentations 56
  - 8.3. Poster Presentations 57
  - 8.4. Degrees Awarded 58
  - 8.5. Funding Generated 58
  - 8.6. Funding Pending 58
  - 8.7. Employment/Research Received 59
    - 8.7.1. Research Awards 59
    - 8.7.2. Research Employment 59
- 9. Conclusions 59
- 10. References 61
- 11. Final Bibliography 64
  - 11.1. Publications 64
  - 11.2. Meetings 64
  - 11.3. Personnel 64

5. Introduction

5.1. NATURE OF THE PROBLEM

While it is hoped that molecular detection and intervention will one day provide a more effective treatment modality, currently, in the words of the Report to the U.S. Army Medical Research and Development Command on the Strategies for Managing the Breast Cancer Research Program, "no dominant etiology for breast cancer has emerged...[this] would lessen the prospects for any quick and easy prevention strategies.... mammography is the method of choice for screening women to detect breast cancer ... mammography has proven to be the most effective means of reducing breast cancer morbidity and mortality."

The primary theoretical limitations of mammography are the system resolution, which determines the minimum size of the detectable malignancy, and the need to expose the patient to ionizing radiation. Using innovative new technology to improve system resolution and reduce required dose will increase the effectiveness of this proven screening modality, with a direct and immediate impact on mortality. In addition, this direct digital system can avail itself of the advantages of digital processing, including improved image contrast and resolution at reduced radiation dose.[1] In practice, mammographic imaging is often limited by quality assurance issues, which can also be favorably addressed by digital processing.

5.2. PURPOSE

The overall objective of this proposal is to develop a mammographic system with extremely high scatter rejection and dynamic range, good resolution and low patient dose. This can be accomplished by developing a direct x-ray detector interfaced with a capillary x-ray optic in an appropriately designed mammographic system.

Kumakhov capillary x-ray optics, invented in the mid-eighties, provide an innovative new way to control x-ray beams. Such optics provide extremely efficient scatter rejection, while allowing beam magnification, demagnification, and shaping to match with the newly developing high efficiency direct x-ray detectors. These detectors owe their high efficiency and resolution to the direct detection of x-ray photons without requiring phosphors for the conversion to visible light. An integrated system of optics and detectors was studied in a highly collaborative effort involving recognized leaders in the fields of capillary optics, x-ray detectors, digital radiology, and mammography. Testing was performed on each of the optics elements independently, and as an integrated unit in a mammographic system.

6. Body

6.1. BACKGROUND

6.1.1. BENEFITS OF DIGITAL MAMMOGRAPHY

Conventional film/screen mammography suffers from limited dynamic range and film granularity, which can reduce the sensitivity of detection of microcalcifications. Digital detection provides high dynamic range, improving contrast, and greatly increasing the tolerance of the final image to under- or over-exposure. Digital images can be enhanced and are amenable to computer aided diagnosis. Spectral information can be included if it is available. Finally, digital images can be quickly transported for skilled consultation.

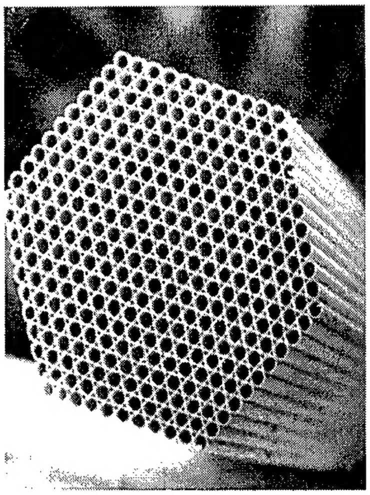

Figure 1. Cross sectional scanning electron micrograph of polycapillary fiber 0.5 mm in diameter.

6.1.2. CAPILLARY OPTICS

Kumakhov capillary optics are bundles of hollow glass capillary tubes with inner diameters as small as a few microns. A typical fiber is shown in Figure 1. X rays incident on the interior of the glass tubes at small angles can be guided down the tubes by total external reflection. The polycapillary fibers guide x rays in a manner analogous to the way fiber optics guide light. Arrays of curved tapered fibers can be used to focus, collimate and filter x-ray radiation.[2,3,4,5,6] Such arrays can be manufactured by stringing hollow glass polycapillaries through metal grids, as shown in Figure 25, or manufactured without grids as a monolithic optic, as shown in Figure 2.

The critical angle for total external reflection of x rays by glass polycapillaries is

$$\theta_c = \frac{\omega_p}{\omega}, \qquad (1)$$

where ω_p is the plasma frequency of the glass, about 30 eV, and ω is the photon frequency. The critical angle is 1.5 milliradians at 20 keV. The x rays can be transmitted in a curved tube so long as the tube is small enough and bent gently enough that the angles of incidence are kept less than the critical angle. For a given radius of curvature, this requires increasingly small diameter tubes as the x-ray energy is raised. In order to avoid the mechanical limitations of such small tube sizes, polycapillary fibers are employed with channel sizes (typically 1-30 μm) much smaller than the outer diameter (300-1000μm).

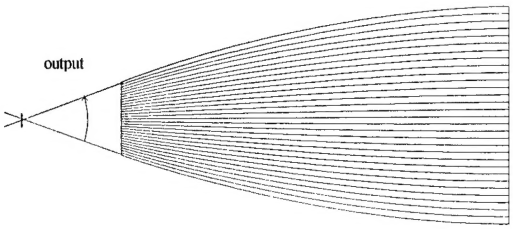

Figure 2 . Monolithic optic geometry.

The use of Kumakhov capillary optics in place of more conventional scatter reduction grids in a mammographic system has significant potential to provide improved resolution, increased contrast enhancement, and reduced dose in mammographic imaging. The optics can also be used to mate the radiographic image with a digital detector by appropriate choice of magnification, demagnification, or separation to discrete chips. In addition, a pre-patient optic could be employed to increase the available intensity in a fan beam relative to simple slot collimation.

6.1.3. DIGITAL X-RAY DETECTION

In almost all radiological systems, detection of x rays is performed by the use of a "phosphor" screen which converts absorbed x rays into visible light photons. The visible light is then recorded on an analog medium, such as film, or detected by a digital detector. The phosphor screen is used because most detectors, including film, are not particularly sensitive to x rays. The use of a screen-film combination reduces radiation requirement compared to direct exposure film by a factor of 50-100.[7] This increase in sensitivity occurs at the expense of resolution. The modulation transfer function of a good film-screen combination drops to less than 0.1 at a frequency of 15 lp/mm.[7] The choice of screen thickness is a trade-off between detected quantum efficiency, which improves with increasing thickness, and resolution, which is degraded by light blur in a thick screen.[8]

Efficient direct x-ray detection virtually eliminates the tradeoff between spatial resolution and sensitivity because of the elimination of the phosphor screen. Direct x-ray detectors can provide resolution of 20 lp/mm or better with nearly 100% Detector Quantum Efficiency (DQE).

An especially promising direct x-ray detector is the cadmium zinc telluride (CZT) semiconductor detector recently developed by Digirad, formerly Aurora Technologies. The DQE of a .5 mm thick CZT detector is essentially unity at 20 keV, while the resolution is to first order independent of thickness. CZT detectors are similar in many respects to cadmium telluride (CdTe) detectors which have been available commercially for many years. The replacement of a fraction of the Cd with Zn causes a wider bandgap and results in a resistivity increase of two orders of magnitude. This high resistivity is an important factor because it reduces leakage current, a significant source of performance degrading noise. Leakage current noise generally limits the use of CdTe detectors by requiring longer integration times and larger pixel sizes.

Another promising direct digital detector is the Charge Injection Device (CID). Like the more common CCD (Charge couple device) CID technology allows for rapid array imaging. Unlike the CCD, the CID is very radiation resistant. Also unlike CCDs, for which the entire array must be read out and simultaneously cleared as a unit, CID pixels can be read individually, repeatedly, and nondestructively, leading to very high dynamic range. CID pixel well depths are also deeper than conventional CCDs, leading to a substantial reduction in blurring from high-energy x-ray photons.

6.2. PROPOSED STATEMENT OF WORK: FINAL ASSESSMENT

I. Development of Capillary Optic Mammographic System: Months 1-36
  I.A. Single Capillary Measurements: Months 1-6: Completed
  I.B. Simulation of Design Strategies: Months 6-18: Completed
  I.C. Assembly and Testing of Prototype Optic: Months 18-24: Completed
  I.D. Design of Final Mammographic Optics and Detector Unit: Months 20-28: Completed
  I.E. Assembly and Testing of Final Optic: Months 28-36: Completed
II. Development of Digital Detector: Months 1-24
  II.A. Fabricate CZT Linear Detector Arrays: Months 1-24: Completed
  II.B. Develop Interconnect Methodology (Wire Bonding): Months 2-8: Completed
  II.C. Assemble and Test Proof of Principle Detector/Multiplexer Hybrid : Months 2-12: Completed
  II.D. Assemble Additional Hybrid Arrays: Months 12-24: Changed
III. Mammographic Measurements: Months 18-48
  III.A. Measurement of Prototype System: Months 18-36: Completed
    III.A.1 Design and Fabrication of Test System: Months 18-24: Completed
    III.A.2. Measure Primary Transmission in a Mammographic Geometry: Months 24-30: Completed
    III.A.3 Measure Transmission of Scattered Radiation: Months 24-30: Completed
    III.A.4. Spectral Measurements: Months 24-30: Completed
    III.A.5. Investigate Artifacts due to Capillary Structure: Months 30-36: Completed
    III.A. 6. Measure Contrast Improvement and Resolution: Months 30-36: Completed
  III.B. Measurement of Final Optics/Detector System: Months 28-48
    III.B.1. Design and Fabrication of Measurement System: Months 28-36: Completed
    III.B.2. Measure Primary Transmission in a Mammographic Geometry: Months 36-42: Completed
    III.B.3. Measure Transmission of Scattered Radiation: Months 36-42: Completed
    III.B.4. Spectral Measurements: Months 36-42: Completed
    III.B.5. Investigate Artifacts due to Capillary Structure: Months 42-48: Completed
    III.B.6. Measure Contrast Improvement and Resolution: Months 42-48: Changed
    III.B.7. Evaluate Image Quality Using RMI Breast Phantom: Months 42-48: Changed

6.3. RESEARCH ACCOMPLISHMENTS

Rather than follow a step by step task listing, this progress report has been divided into subject areas to provide a more coherent description of the current state of the art. While there were substantial manufacturing delays in the production of monolithic optics, the available optics have lent themselves to a thorough systematic review of the various optics geometries proposed for this project. Representative measurements have been made on a large number of optics geometries, rather than relying on the simple simulations initially proposed for this project. Manufacturing issues are discussed as well. A decision has been made to concentrate on two geometries, a collimating optic, and a “multi-taper” post patient optic assembled of three smaller tapers to produce a larger area optic without the technological problems of a single large area glass bundle. Manufacturing delays have led to a granted no cost extension of this project.

The proof-of-principle linear CZT array has been demonstrated, but an alternate detector path, CID technology appears equally promising. Studies of both detectors are discussed.

6.3.1. POLYCAPILLARY OPTICS

Measurements and simulations have been performed on several geometries: single fibers; multifiber collimating optics; multifiber straight antiscatter optics; and magnifying and demagniying monolithic optics.

6.3.1.1. SINGLE FIBERS

6.3.1.1.1. Transmission

An important step in optics development was the breakthrough in modeling capacity, which has led to an unprecedented level of theoretical understanding of the basic properties of polycapillary fibers, especially fiber defects. To evaluate the experimental performance of polycapillary fibers, and design capillary optics, it is necessary to be able to predict theoretical behavior for complex geometries. The modeling program for single fibers is based on a Monte Carlo simulation of simple geometrical optics. The computational speed is greatly enhanced by a reduction to two dimensions by projecting the trajectory onto the local fiber cross-section.[9] Reflectivities are computed from standard tables.[10] Significant recent progress has been made in understanding the effect of capillary profile error, waviness, and roughness on the transmission spectra.[11] This is extremely important in providing feedback to the manufacturing process. It has been found that extremely good fits can be produced with

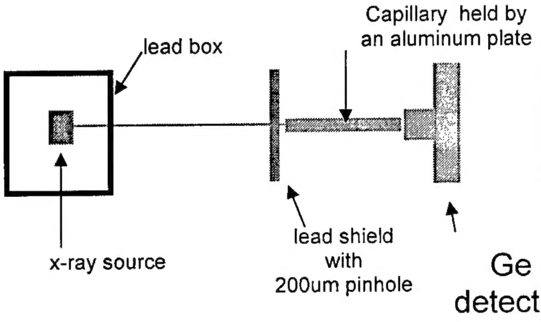
Capillary held by an aluminum plate
lead box
x-ray source
lead shield with 200um pinhole
Ge detector

Figure 3. Experimental setup.

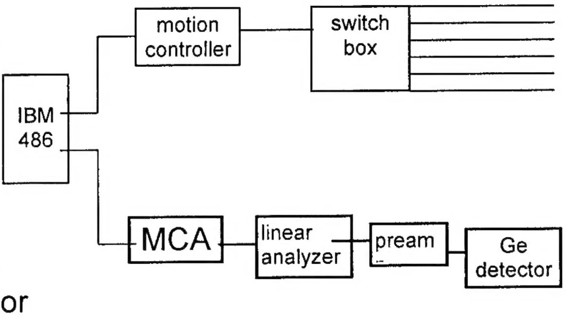

Figure 4. Electronic system.

Type	Description	Outer Diameter, mm	Channel Size, μm	Open Area	Length, mm
A	Borosilicate	0.5	12	65%	105
B	Lead glass	0.5	12	52%	95
C	Borosilicate	0.75	22	50%	136
D	Borosilicate	4	12	55%	130
E	Borosilicate	0.3	4-5	55%	105

Table 1. Description of polycapillary fibers.

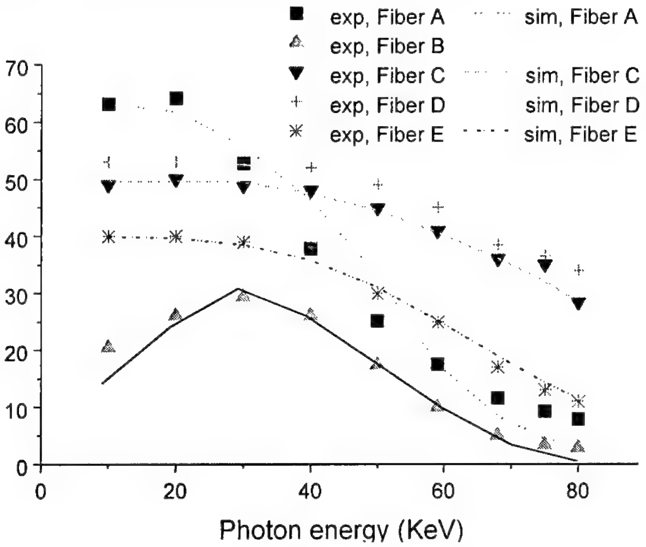

Figure 5. Measured transmission versus energy for polycapillary fibers listed in Table 1.

only two fitting parameters if a more physical model of waviness is employed.[12]

The experimental arrangement for single capillary measurements is shown in Figure 3 and Figure 4. An optical rail affixed to an optical table carries an x-ray source, fiber platform, and x-ray detector. Each can be positioned independently in three dimensions. A collimator is placed before the fiber and any remaining x-ray leakage around the fiber is eliminated with metal powder or filings. The measured fibers are described in Table 1.

The results of transmission studies as a function of photon energy are shown in Figure 5.[13,14] All of the fibers except the lead glass have transmissions at 20 keV nearly equal to their fractional open area (the fraction of the cross section of the capillary which is open space, the rest being glass walls). This transmission corresponds to the primary transmission expected for a linear capillary optic employed as an antiscatter grid.
The transmission falls off at higher energies. Modeling this transmission spectra has lead to a greater understanding of defects in polycapillary optics.

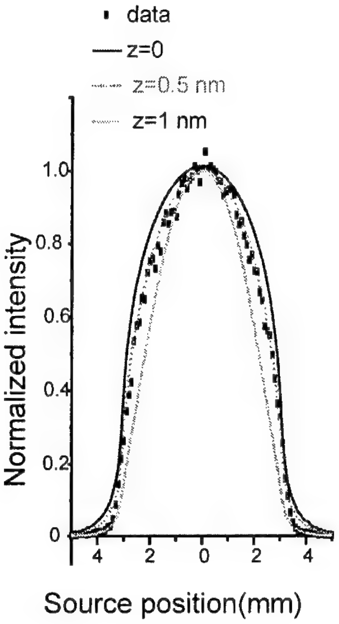

Figure 6. Source scans at 10 keV.

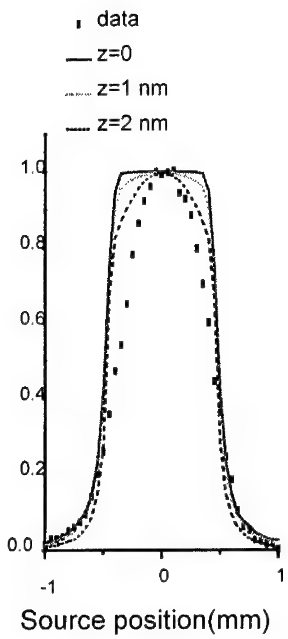

Figure 8. Source scans at 68 keV.

In Figure 6, simulations with or without roughness corrections are compared with the experimental data. In these measurements the source is scanned transverse to the fiber axis. The simulation with a roughness height of 0.5 nm fits the experimental data quite well. It is definitely over-corrected when the roughness is 1.0 nm. The same simulations, shown in Figure 8, are also carried out at 68 keV, where the width of the curve is narrower than that at 10 keV because of the smaller critical angle. As a result, photons also experience fewer bounces on average. Simulations with roughnesses as large as 1.0 and 2.0 nm still could not fit the data. Knowing that 1.0 or 2.0 nm roughness is definitely too large at 10 keV, we can determine that the roughness correction by itself is not sufficient at high energy to reproduce source scan measurements. Other effects need to be considered. These are bending and waviness.

A slight bending of the capillary can dramatically reduce the transmission of high energy photons because of the small critical angle. A comparison between experimental data and simulations with different bending is shown in Figure 7. The figure shows that the simulations with bending alone do not fit the experimental data well, which indicates that bending is not the only factor which causes the high energy transmission to drop. However, from Figure 7, we can see that the range of the bending radius must be larger than 100m to give the observed transmission at the highest energy(80KeV).

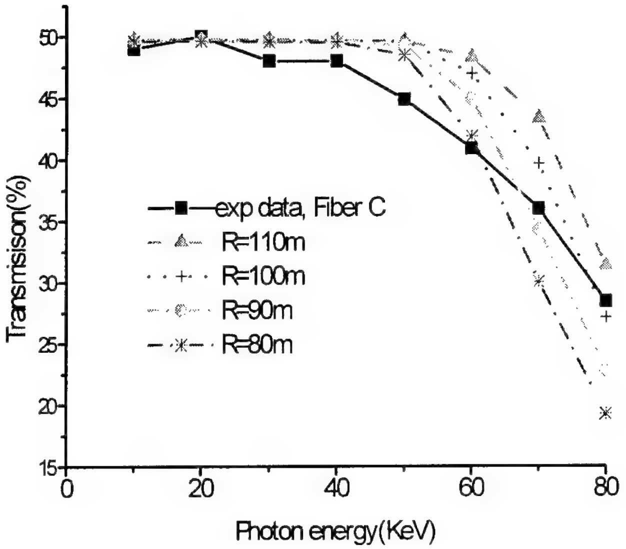

Figure 7. Transmission spectra of Fiber 3 simulated with different bending curvature alone and compared with experimental data

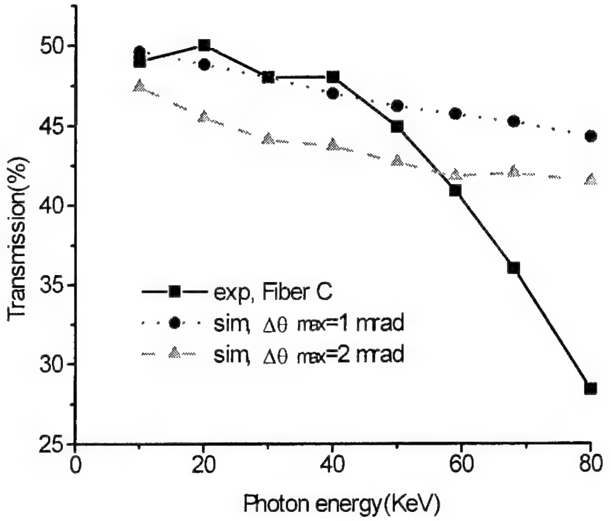

Figure 9. Simulations of transmission spectra with waviness only compared with the experimental data.

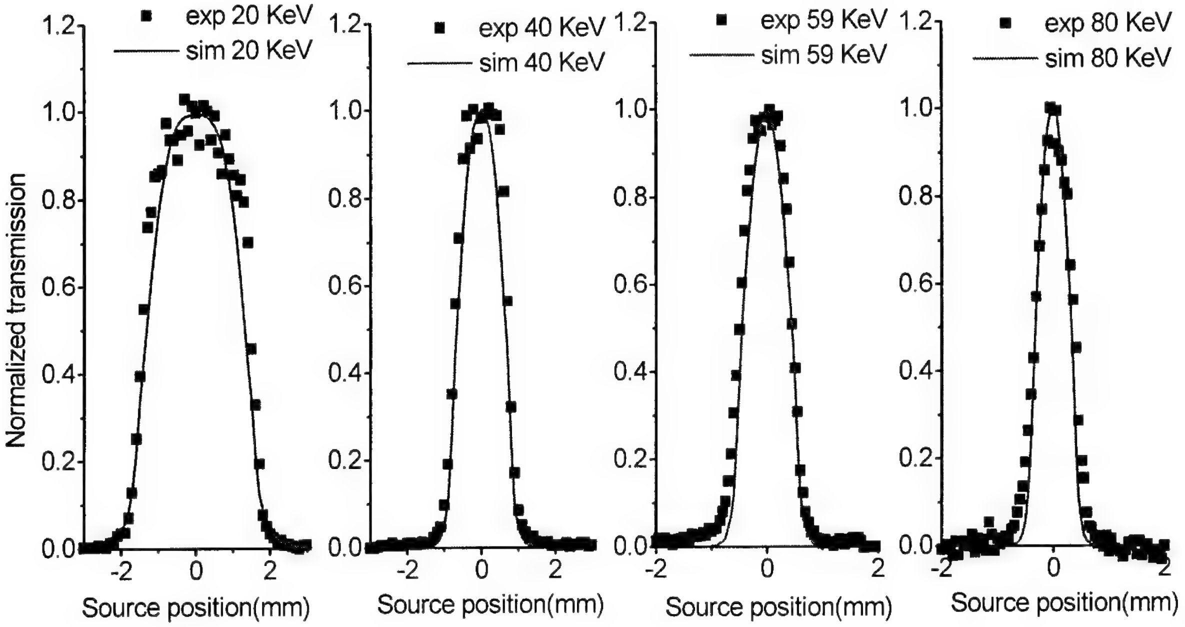

Figure 10. Simulated source scan curves compared with experimental data at four different photon energies. Parameters are: $R = 125$ m, $\Delta\theta max = 0.35$ mrad, roughness height=0.5 nm.

Capillary surface oscillations with wavelengths shorter than the capillary length and longer than the wavelength of the roughness are called waviness. The detailed shape of waviness is unknown. Its average effect can be considered as a random tilt of the glass wall, so that the grazing angle of the photon is changed by a random amount, $\delta\theta$, after every bounce. $\delta\theta$ is a random number between $-\Delta\theta_{max}$ and $\Delta\theta_{max}$ if $\theta \geq \Delta\theta_{max}$. The maximum random tilt angle $\Delta\theta_{max}$ is an adjustable parameter which depends on the waviness of the polycapillary fiber To keep θ' positive, $\delta\theta$ is taken to be a random number between $-\theta$ and $\Delta\theta_{max}$ when $\theta < \Delta\theta_{max}$. Since a photon with a incident angle smaller than $\Delta\theta_{max}$ has a larger chance to experience an angle increase than an angle decrease, this is physically reasonable. In Figure 9, simulations with waviness corrections with $\Delta\theta_{max}$ set at 1 mrad and 2 mrad, which is comparable to the critical angle, are compared with the

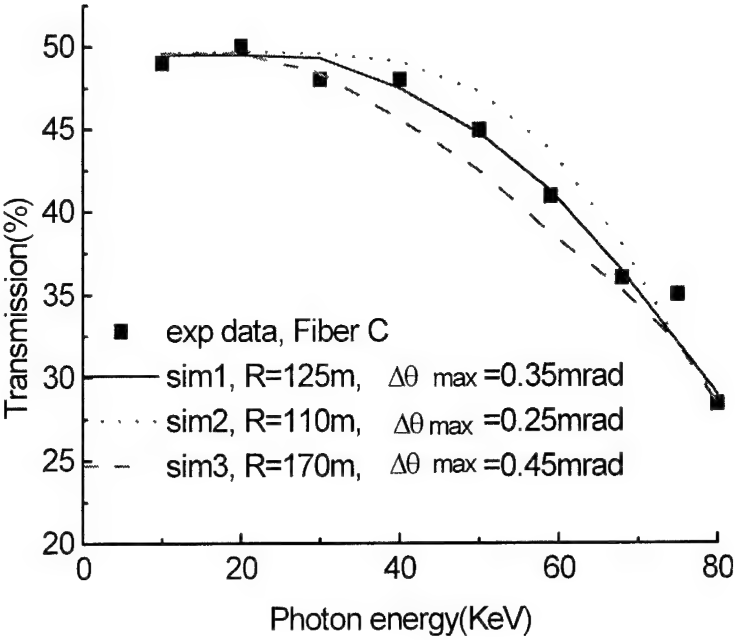

Figure 11. Simulated transmission spectra with different bending and waviness compared with the experimental data in search for the best fitting of Fiber C.

experimental data. This figure shows that simulations with waviness alone do not fit the experimental data. This is because the waviness correction changes the reflected angle, not the profile. In fact the capillary is still considered to be straight, so those photons which have few reflections will not be significantly effected by waviness.

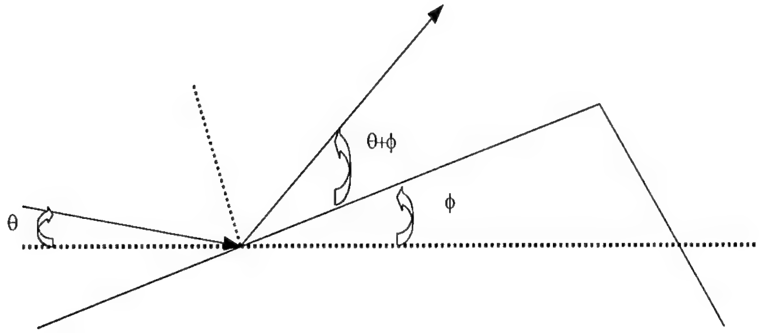

Figure 12. Scheme of an x-ray beam interacting with a random tilt surface.

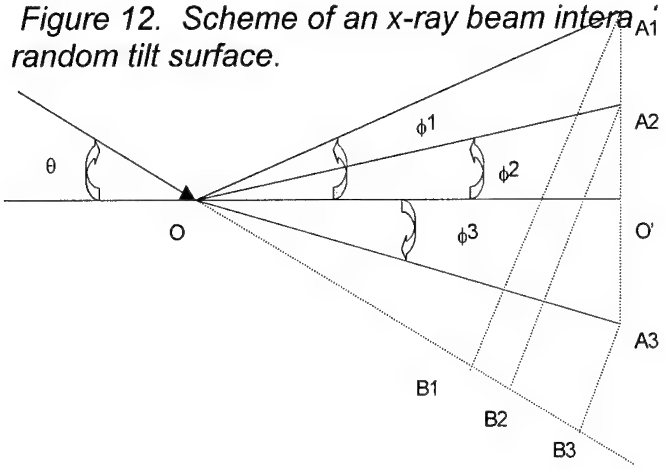

Figure 13. Three surfaces, OA1, OA2 and OA3, with different tilt angles, $\phi 1$, $\phi 2$ and $\phi 3$, respectively, from the nominal surface OO'.

Finally the waviness and bending are combined by increasing the bending radius R, roughly determined in Figure 7, and adding a waviness parameter, $\Delta\theta$max. Several trials are shown in Figure 11. Sim2 has too much bending and not enough waviness; sim3 has too much waviness and not enough bending; sim1 is the best fit. Roughness is also included in those simulations. The source scan simulation with the three fixed parameters are plotted along with the experimental data in Figure 10 for four more photon energies. They all fit quite well. This model, hereafter labeled M1, assumed a uniform distribution of tilt angles, which is not quite physical. In more recent work, discussed as Model M2, it is assumed that these tilt angles, ϕ, are normally distributed in the range $(-\pi/2, \pi/2)$ with the mean value equal to zero. For high quality optics, the standard deviation of this normal distribution, σ, is much smaller than the critical angle, θ_c. The probability distribution of tilt angles, ϕ, is

$$G(\phi) = \frac{1}{\sigma\sqrt{2\pi}} e^{-\frac{\phi^2}{2\sigma^2}}. \tag{2}$$

In this work, Model M2, consideration was taken of the fact that the surface tilt angle will affect the probability of x-ray impact on that surface. Taken to extremes, a surface region perpendicular to the beam is much more likely to intercept the beam than a surface region parallel to the beam. Figure 13 displays three surfaces, OA_1, OA_2 and OA_3, with different tilt angles, ϕ_1, ϕ_2 and ϕ_3, respectively, from the nominal surface OO'. The projections onto the nominal surface for the three surfaces are equal, $OA_1{*}\cos\phi_1 = OA_2{*}\cos\phi_2 = OA_3{*}\cos\phi_3 = OO'$. The probability of incidence of a parallel x-ray beam with incident angle θ (with respect to the nominal surface OO') hitting these tilted surfaces is given by their corresponding perpendicular length A_jB_j (for j = 1, 2 or 3)

$$P_j \propto A_jB_j = OA_j \cdot \sin(\theta+\phi_j) = \frac{OO}{\cos\phi_j}\cdot \sin(\theta+\phi_j), \tag{3}$$

We call this the tilt-corrected probability distribution. The complete description of this distribution is

$$H(\phi) = \begin{cases} \dfrac{F\sin(\theta+\phi)}{\cos(\phi)}, & -\theta < \phi < \dfrac{\pi}{2} \\ 0, & -\dfrac{\pi}{2} < \phi \le -\theta \end{cases} , \tag{4}$$

where θ is the incident angle, ϕ is the tilt angle and F is a normalization constant.

Combining the normal distribution G(ϕ) with the tilt correction H(ϕ) gives ϕ for a certain incident angle θ as follows:

$$J(\phi) = \begin{cases} Ke^{\frac{-\phi^2}{2\sigma^2}} \cdot \dfrac{\sin(\theta+\phi)}{\cos\phi}, & -\theta < \phi < \dfrac{\pi}{2}, \\ 0, & \dfrac{-\pi}{2} \le \phi \le -\theta \end{cases} \tag{5}$$

where θ is the incident angle, ϕ is the tilt angle and K is a normalization constant.

Noting that

$$\frac{\sin(\theta+\phi)}{\cos\phi} = \sin\theta + \cos\theta \cdot \tan\phi , \tag{6}$$

and that both the incident angle, θ, and the tilt angle, ϕ, are very much less than 40 mrad, we use the approximation

$$P(\phi) = \begin{cases} Ce^{\frac{-\phi^2}{2\sigma^2}} * (\theta+\phi), & -\theta < \phi < \dfrac{\pi}{2}, \\ 0, & -\dfrac{\pi}{2} \le \phi \le -\theta \end{cases} \tag{7}$$

where the normalization constant , C, is

$$C \approx \frac{1}{\sqrt{2\pi}\,\theta\sigma + 2\sigma^2}, \tag{8}$$

to speed the calculation. P(ϕ) is called the tilt-corrected normal distribution. In model M2, σ is the variable that describes the amount of waviness. An example of J(ϕ) and P(ϕ) is shown in *Figure 14*. The result of the waviness calculation is shown in Figure 15. The model M2 shows a much larger drop at high photon energies for lower values of the waviness than does model M1.

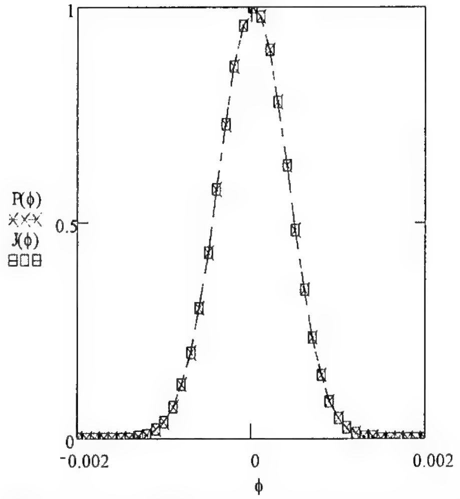

Figure 14. P(ϕ) and J(ϕ) versus tilt angle ϕ when incident angle θ = 0.009rad, standard deviation σ = 0.0004rad. ϕ is in rad.

A comparison of the simulation with bending and waviness to the experimental data is shown in Figure 16.

Using a similar technique, the simulation was compared to the fibers listed in Table 1, using the parameters listed in Table 2. The results are plotted in *Figure 17* and *Figure 18*. In *Figure 17*, the transmission for fiber A shows a rapid drop for energies above 30 keV. Although fiber D has lower fractional open area than fiber A, its transmission exceeds that of fiber A at energies above 30 keV. This is because fiber A is thin (0.5 mm in outer diameter) and flexible, therefore difficult to keep straight in the measurement apparatus. Model M2, which can vary only bending and waviness, requires a much sharper bend for fiber A than for fiber D. This bending is more significant at high energies, where the critical angles are smaller.

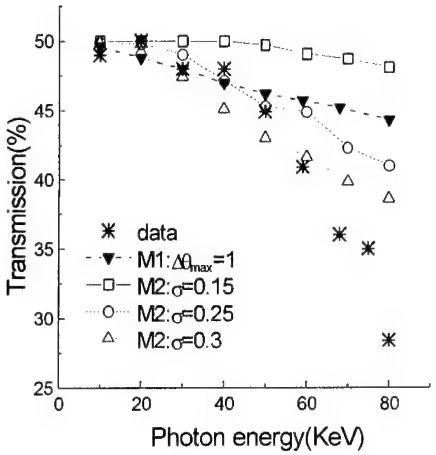

Figure 15. Simulations of transmission spectra for fiber C with only waviness compared with the experimental data. This figure shows the effects of waviness. It also shows simulations using waviness alone do not fit the data. The simulations do not include roughness or bending.

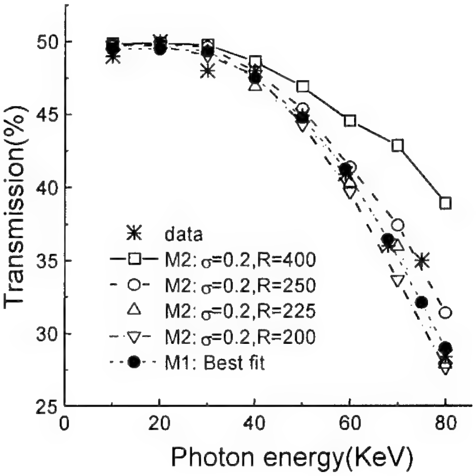

Figure 16. Simulated transmission spectra using model M2 with fixed waviness (σ=0.2 mrad) and different bending (bisection method), compared with the experimental data. The simulation curves shown are just a few representative cases in the bisection process. For M2, the best-fit parameters are σ = 0.2 mrad and R = 225 m; for M1, they are z = 0.5 nm, s = 6 μm, $\Delta\theta_{max}$ = 0.35 mrad and R = 125 m.

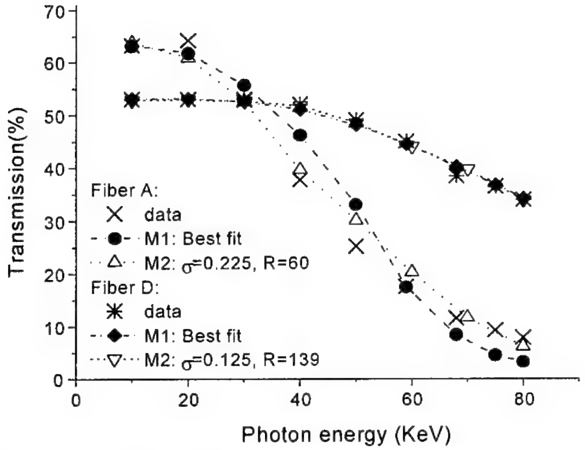

Figure 17. Simulations of transmission spectra of fiber A and fiber D with their best-fit parameters compared with the experimental data. All parameters related to this figure are listed in Table 1.

Transmission curves for fiber C and D are similar in shape and are nearly flat up to 60 keV, as shown in *Figure 18*. However, the smaller channel size for fiber D results in the simulation being less sensitive to bending. Therefore a larger bending curvature (smaller radius) is required for fiber D. The waviness correction for fiber D must therefore be smaller to keep the transmission about the same as for fiber C.

Fiber E is the thinnest fiber. Table 2 shows that it has the largest bending correction because of its flexibility. Its transmission curve is flat up to 40 keV. This is due to its very small channel size, as discussed in the comparison of fiber C and fiber D. However, if the channel size is too small, as in fiber E, it also results in more reflections being needed for a photon to traverse the fiber and may have introduced other defects such as blocked channels. This is why the transmission is only 40% for the energies below 40 keV although the open area is around 55%.

The new model yields as high a quality fit with two fewer fitting parameters than used in model M1 in Figure 5. The high transmission and the simulation results show that the quality of the capillary fibers is quite good. The bending radius is above 130 meters for type 3 and type 4 capillaries. It is hopeful that we can further improve the high-energy transmission performance of polycapillary fibers by decreasing to an optimum channel size, and making them more rigid.

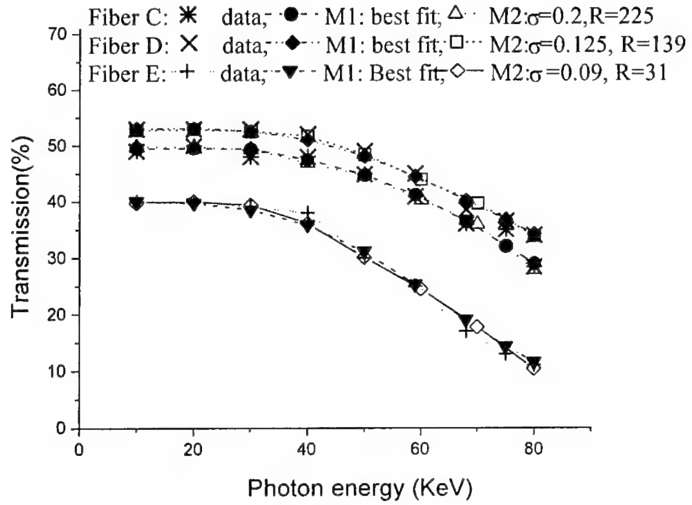

Figure 18. Simulations of transmission spectra of fiber C, fiber D and fiber E with their best-fit parameters compared with the experimental data. All parameters related to this figure are listed in Table 2.

Fiber Description						Model M1				Model M2	
Fiber #	Type	Outer Diameter (mm)	Channel Size (μm)	Area	Length (mm)	z nm	s μm	R m	$\Delta\theta_{max}$ mrad	R m	σ Mrad
A	1	0.5	12	65%	105	0.7	6	105	0.4	60	0.225
C	3	0.75	22	50%	136	0.5	6	125	0.35	225	0.2
D	4	4	12	55%	130	0.8	6	110	0.285	139	0.125
E	5	0.3	4-5	55%	105	0.7	6	28	0.2	31	0.09
F	4	4	12	55%	130	0.8	6	90	0.45	90	0.18

Table 2 *Parameters for best-fit simulations. R is the bending radius. For M1, $\Delta\theta_{max}$ is the amount of waviness, z is the roughness height and s is the roughness correlation length. For M2, σ is the standard deviation of the waviness.*

Fiber B in Figure 5 has poor transmission; it is a lead glass fiber, with high surface roughness and waviness. More recently, higher quality lead glass fibers have been produced. The transmission as a function of photon energy for these fibers is shown in Figure 19. These leaded fibers have higher absorption of high angle photons than the lower density borosilicate glass fibers, and therefore would provide even better scatter rejection, as is described in section 6.3.1.3.2.4.

Transmission was also measured of deliberately curved fibers, which can be used to deflect x-ray beams over larger angles. The results are shown in Figure 20. Simulated transmission for a single fiber with various channel sizes is shown in Figure 21.

6.3.1.1.2. Absorption Measurements

To achieve total scatter

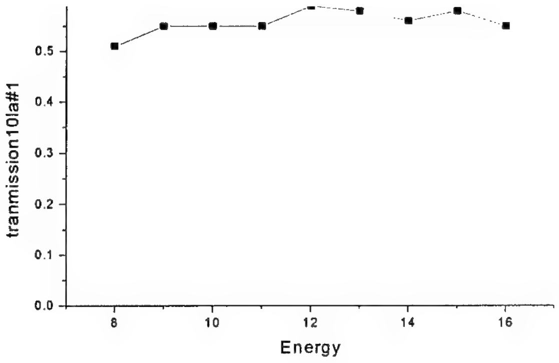

Figure 19. Recently manufactured lead glass fibers.

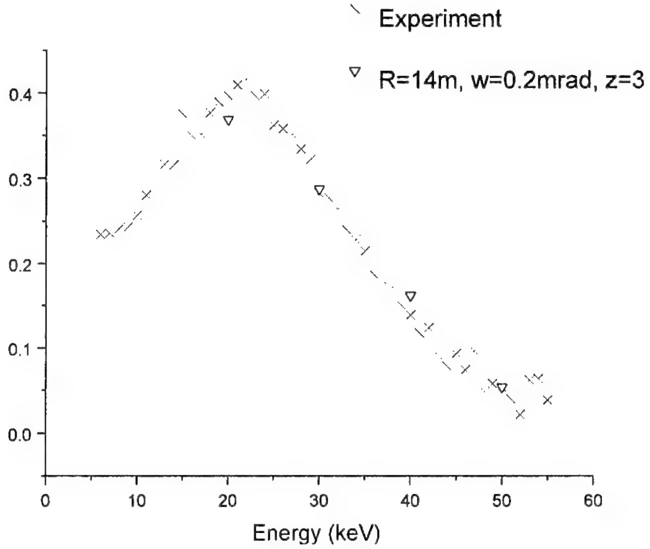

Figure 20. Transmission efficiency of 350 μm OD polycapillary fiber with 6 μm channel diameter. The fiber length is 25 cm. Simulated values are shown for 20, 30, 40, 50 keV x rays. The parameters are curvature, R; waviness, w; and roughness, z.

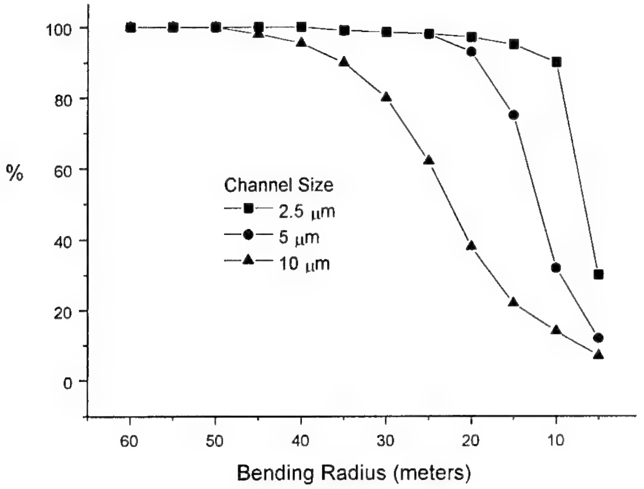

Figure 21. Simulated transmission as a function of bending radius at 50 keV, with no waviness or roughness.

rejection, the glass wall of the optics must be thick enough to absorb the scattered x rays from various directions while allowing the majority of the primary x rays to pass. The absorption of the polycapillary fiber bundle was measured by tilting the optic to an angle which is larger than the critical angle.

The setup includes a source, a pinhole with size of 200 μm, an aluminum plate which is used to hold the capillary bundle, and a Germanium detector. The source has a maximum operate voltage of 100 kV. The source and aluminum plate are attached on linear stages which are controlled by linear actuators. Both the source and the optics fiber can move freely in two perpendicular directions transverse to the x-ray beam. An additional rotary stage is used to rotate the aluminum plate, so that the optic can also be rotated in horizontal direction.

The experiment starts with the alignment between the source, pinhole, and detector, by adjusting the source and fiber positions. After alignment, the optic was tilted to an angle larger than the largest critical angle for the measured energy range, then translated out of the x-ray beam. While the capillary optics was moved into the x-ray beam step by step, an x-ray spectrum was taken by the germanium detector after the optics at each step. The acquire time for each step was 30 seconds. The transmission at every step is the ratio between the counts without optics and the counts with optics at that step. Transmission at different energies as a function of optic position is plotted in Figure 22 along with the theoretically calculated values.

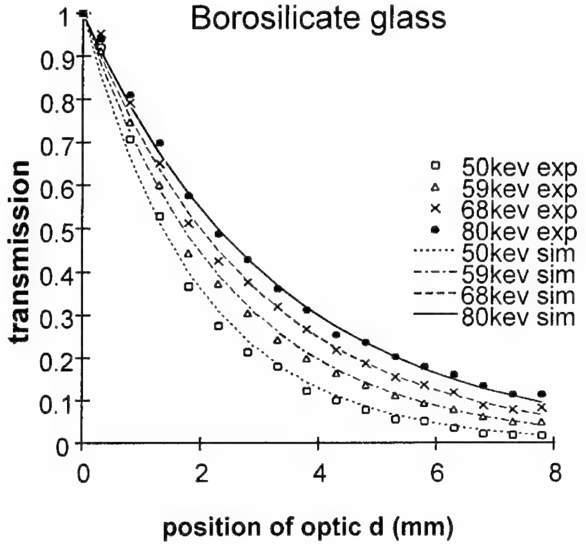

Figure 22. Absorption measurement

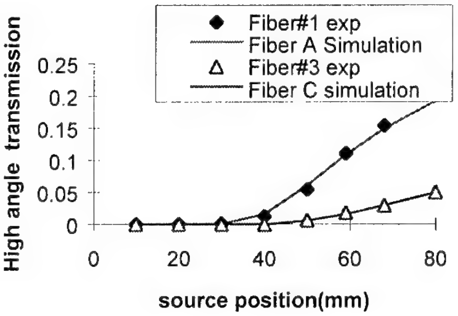

Figure 23. High angle transmission through capillary walls as a function of photon energy.

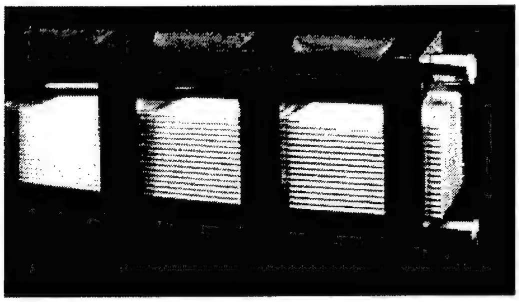

Figure 25. Multifiber collimating lens.

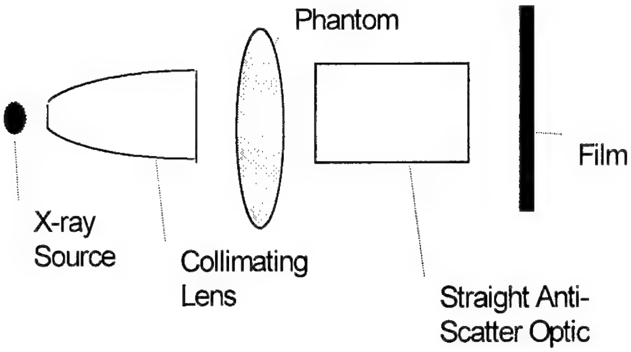

Figure 24. Set-up for Anti-scatter measurements.

Large angle transmission can be calculated as

$$T_s = e^{-(1-f)\cdot\mu\cdot\rho\cdot x} \tag{9}$$

where μ is the mass attenuation of the material which can be calculated from tabulated values[21] according to the mass composition, ρ is the density of the glass, f is the open area of the capillary bundle, and x is the distance that the x-ray beam travels across the fiber. x can be calculated from capillary movement d and capillary tilting angle,

$$x = d / \alpha\,, \tag{10}$$

where α is the tilting angle in rad. Theoretical calculated numbers from equation (9-10) are compared with the experimental result in Figure 22. The theoretical values fit well with the experimental data. Measured and theoretical transmission of a polycapillary fiber as a function of photon energy is shown in Figure 23. This "high angle transmission" corresponds to scatter transmission for the capillary optics used as an antiscatter grid, and is less than 1% at 20 keV. The solid lines are theoretical calculations, which agree quite well with the data. Lead glass optics would have even better scatter rejection, as shown in Figure 26.[15]

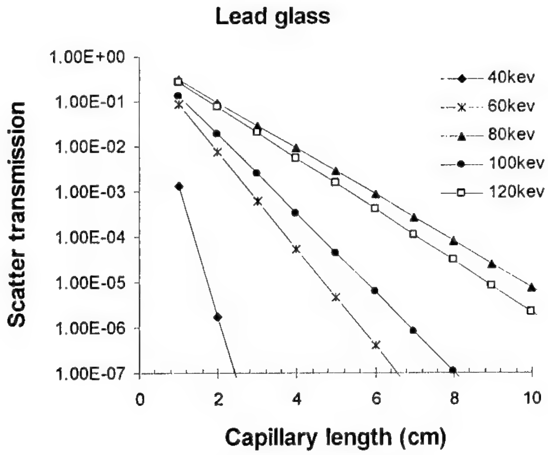

Figure 26. Calculated scatter transmission for lead glass optics of various lengths.

6.3.1.2. COLLIMATING OPTICS

6.3.1.2.1. 8 keV Prototype

6.3.1.2.1.1. Transmission and Uniformity

Because of the technological difficulties in producing large area monolithic optics, the fastest route to a large scale antiscatter system for contrast measurements is a straight optic.

The low angular acceptance of the capillary channels requires that such an optic be used with a collimated beam, as shown in Figure 24. A collimating lens, similar to that pictured in Figure 25, and a straight fiber bundle of 3 cm diameter were obtained. The collimating lens has an output diameter of 3 cm, a focal distance of 150 mm, and collects from an angle of 8°. It was designed for 8 keV, where the transmission is 30%, but has a transmission of 14% at 20 keV. The reduced transmission is due to the reduction in critical angle for reflection with x-ray energy, as stated in equation (1). Because this optic would be used prepatient, low transmission would not increase dose, only increase tube loading. More importantly, as will be demonstrated in the next sections, a lens actually designed for 20 keV would have a higher transmission at that energy. The primary purpose of studying this lens is to develop experience with large scale polycapillary optics and refine the modeling to increase the confidence in the simulations. The simulated and measured transmission of the lens as a function of source to lens distance is shown in Figure 27. The simulation, which models the complex geometries of complete lenses, was developed by X-ray Optical Systems, Inc. Some delay in the commencement of the simulation task was created by the necessity of assuring the confidentiality of the proprietary code while providing access to student researchers. Access was provided, and comparisons of measurements and simulations of a collimating lens have given good results. The measured and simulated transmission as a function of photon energy for the lens (with the central part blocked, as shown in Figure 28), is shown in Figure 32.

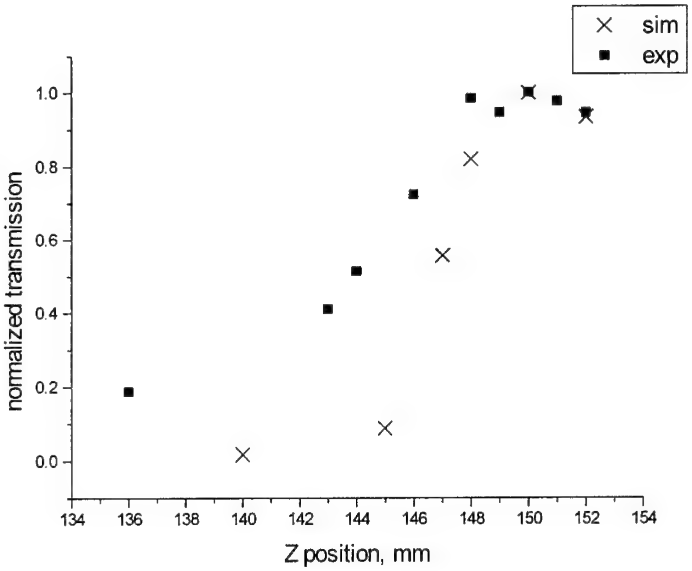

Figure 27. Variation in measured (box) and simulated (x) 20 keV transmission as the source is moved towards the lens along the fiber axis.

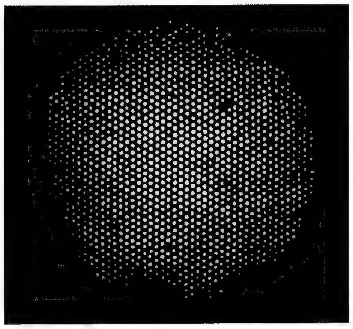

Figure 29. X-ray photograph of output of collimating optic.

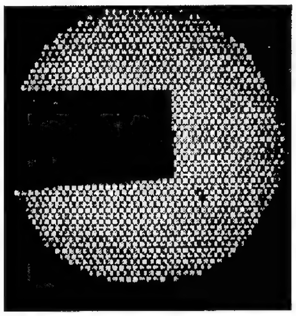

Figure 28. X-ray photograph of output of 8 keV collimator. A rectangular lead sheet

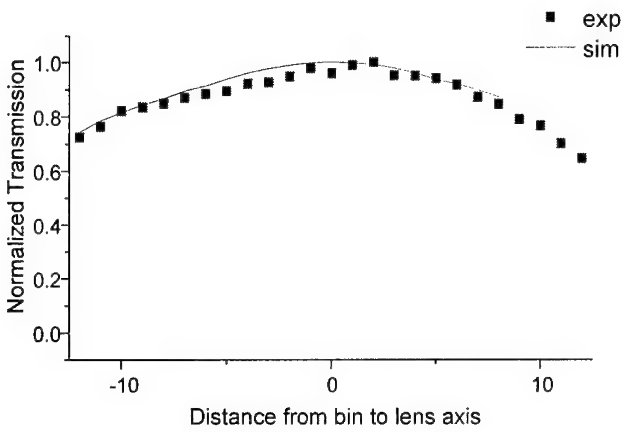

Figure 30. Measured and simulated local transmission of the prototype collimating lens, at 8 keV. Transmission variation is less than 6%.

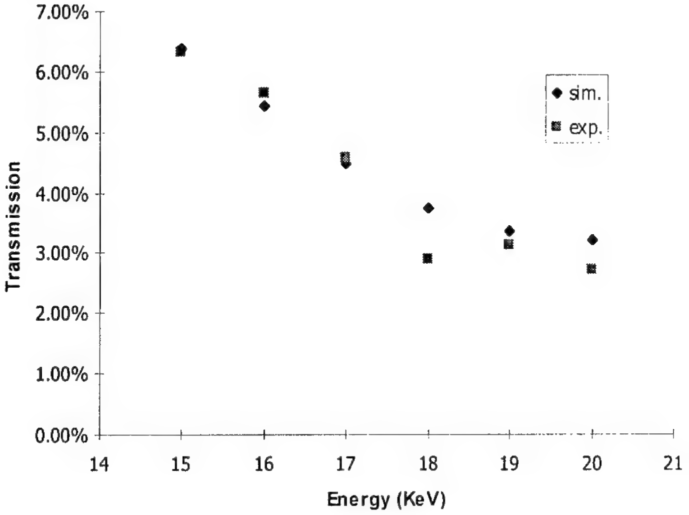

Figure 32. *Transmission of 8 keV collimator as a function of photon energy. The simulation assumes a fiber open area of 65%, the fibers packed to fill 50% of the lens input area, and ¼ of the lens blocked by the lead shield.*

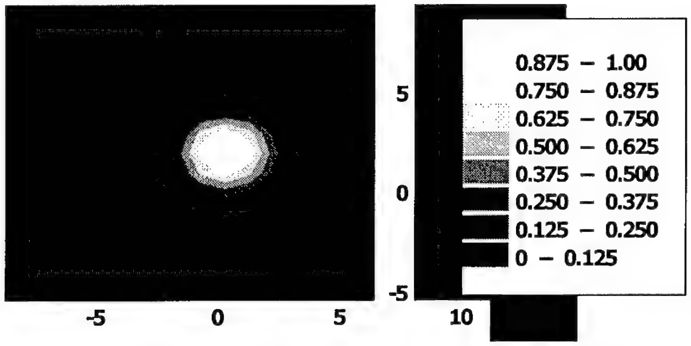

Figure 31. Simulated output, at 20 keV, of collimator designed for 8 keV.

More serious for imaging experiments than the low transmission of a lens designed for lower energies, is the non-uniformity of the field. The outer fibers are bent too much to permit good transmission at these energies. The fall off in transmission can be seen in the photograph shown in Figure 29, and in the simulation of Figure 31. Contrast enhancement measurements must take these nonuniformities into account. The uniformity is much better at the design energy, as shown in Figure 30. The simulation accurately predicts the field uniformity. Figure 28 shows the output of the lens after a center section was blocked. This section contains fibers which were removed for study of radiation exposure effects after extensive exposure to intense synchrotron radiation.[16,17] The radiation effects were found to be manageable and are not expected to be significant for mammography.

The aligned transmission measurements of *Figure 32* are important to determine the collection efficiency of the lens. Variation in transmission as a function of entrance angle is important for estimating the scatter rejection properties of other optics which might be used post patient. This variation was measured by first aligning the source with the lens and then moving the source in the plane transverse to the capillary axis. The transmission efficiency decreases when the x-ray source is moved off-axis because the angle between the x ray and the reflection surface of the capillary increases. Because the reflectivity decreases sharply with

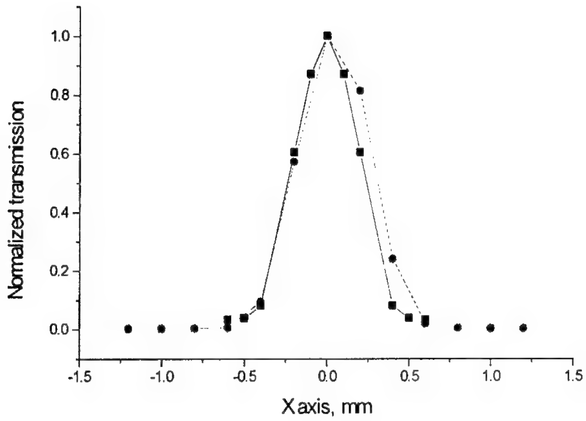

Figure 33. Transmission of a multifiber collimating lens as the source is moved transverse to the lens axis. Circles are measured data, and boxes simulation results.

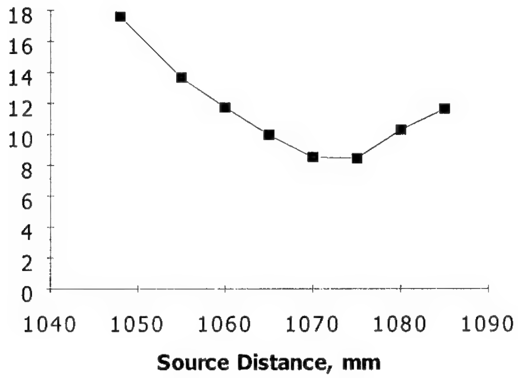

Figure 36. Width of scan of transverse source scan, as a function of source motion along the lens axis, for collimating lens, measured at 20 keV.

angle this produces greater loss at each reflection. In addition, x rays traveling through the capillary at a larger angles undergo more reflections. A comparison of measured and simulated data, with good agreement, is shown in Figure 33. Variation in the width of the scan as a function of the lens to source distance is also used as the primary method of determining both the focal distance of the lens, and the depth of field. The measured variation is plotted in Figure 36. The depth of field can be seen here and also in Figure 27, which shows the measured and simulated transmission as a function of source to lens distance. The depth of field is about 11 mm.

6.3.1.2.2. Divergence and Diffraction Gain

Measurements of the exit divergence of the collimating optic have been performed at 8 keV and at 20 keV. Exit divergence is important if a capillary optic is to be used as a collector fore slit before the patient.

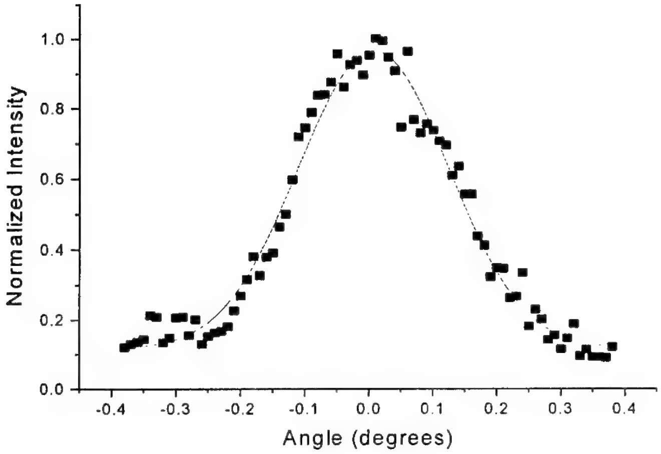

Figure 34. Output divergence of the 8 keV collimating lens, measured at 20 keV.

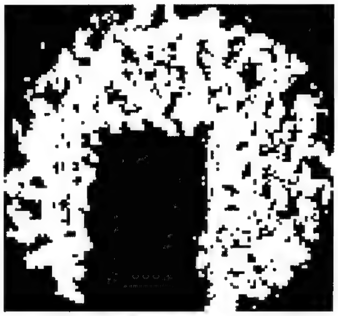

Figure 35. Image of lens shown in figure 30, taken 30 cm after the lens.

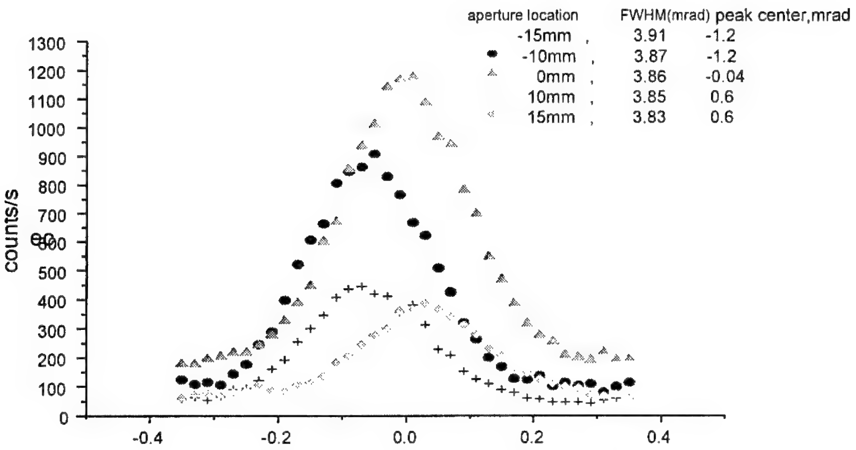

Figure 37. Measured local divergence of the output of multi-fiber I at 8 keV.

In this case, the spatial resolution will depend on the angular spread of x-rays at the exit end of the polycapillary fibers. Large angular divergence is equivalent to a large focal spot size in a conventional system. The divergence, measured by rotating a silicon wafer in the beam and measuring the width of the diffraction curve, is shown in Figure 34. The full width of the divergence measured at 20 keV is 2.56 mrad, slightly greater than the critical angle for total external reflection. The effect of the divergence is shown in Figure 35, in which the image of the fiber bundle walls have been blurred by placing the film 30 cm behind the lens.

The ability of the optic to redirect the collected x rays into a beam of relatively low divergence means that the reflection efficiency off a monochromatic crystal is greatly enhanced. While the low power test source was not intense enough to permit imaging after monochromatizing, measurements were made of crystal reflectivity. A silicon (100) crystal was found to reflect approximately .0047% of the beam from the molybdenum source after collimation. This is in reasonable agreement with a calculation[18] of expected reflectivity for a crystal with 0.14 mrad mosaicity, which is reasonable for the crystal used. The gain, relative to no collimation, is on the order of 100x.

The divergence can also be used to assess fiber alignment in the lens. The beam exiting the optic is characterized by a divergence that arises from two effects. The first is the local divergence of the x-rays emerging from each channel, usually between θ_c, the critical angle for total reflection and $2\theta_c$. There is also fiber misalignment, the deviation of the individual channel axis direction from the optic axis direction. Local divergence depends upon the surface roughness,[19] waviness, and bending of fibers through the optic. Figure 37 shows the measured local divergence of the

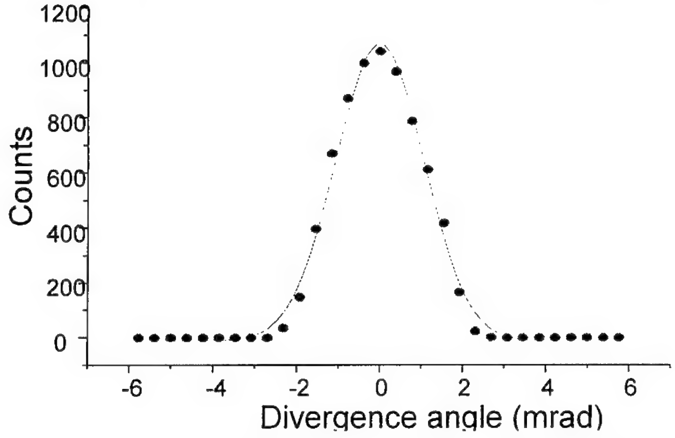

Figure 38. An ideal whole lens simulation at 8 keV gives a divergence FWHM of 2.5 mrad.

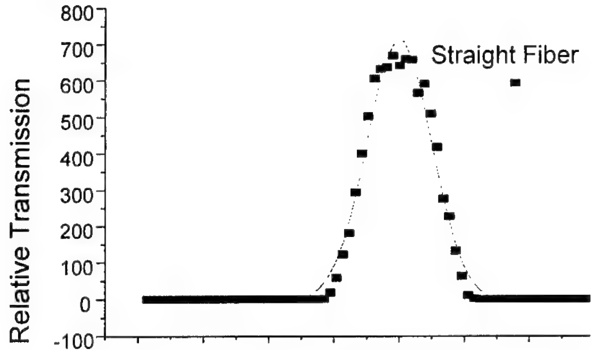

Figure 39. For an ideal fiber (with no surface defects), the divergence simulation yields a FWHM of 2.36 mrad at 8 keV.

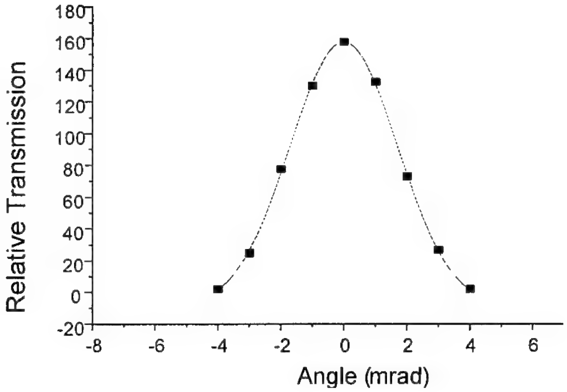

Figure 40. A simulation with a waviness of 0.15 mrad increases the divergence value from 2.4 mrad for an ideal straight fiber to 4.0 mrad.

output of the collimating lens at 8 keV with the aperture at –15 cm, -10 cm, 0 cm, 10 cm and 15 cm off the axis of the lens. The FWHM of each divergence curve is in the range of 3.8 mrad to 3.9 mrad, which is very close to the critical angle of about 4 mrad at 8 kev. The peak centers of these five local divergence curves are systematically shifted. This shift could be caused by the output ends of the fibers inside the lens being slightly convergent rather than parallel. The widths of the measured local divergence curves shown in Figure 37 are larger than that predicted by an ideal lens divergence simulation, shown in Figure 38.

The divergence of the modeled ideal lens is low because the nearly straight central fibers, if ideal, would not increase the divergence above the entrance divergence due to the source spot size. Figure 39 shows the simulated divergence profile of x-rays exiting from an ideal straight fiber, which has a FWHM of 2.36 mrad.

The simulations in Figure 38 and Figure 39 did not include the effects of profile defects and waviness. Waviness will increase the angle of reflection for x-ray photons for most bounces inside the channel. Consequently the divergence from the lens increases. Fig 19 shows a simulated transmission of a straight fiber as a function of exiting angle, using a waviness of ω = 0.15 mrad. The width of the simulated divergence curve for this straight fiber is about 4.0 mrad, which is close to the local divergence at the center of the lens

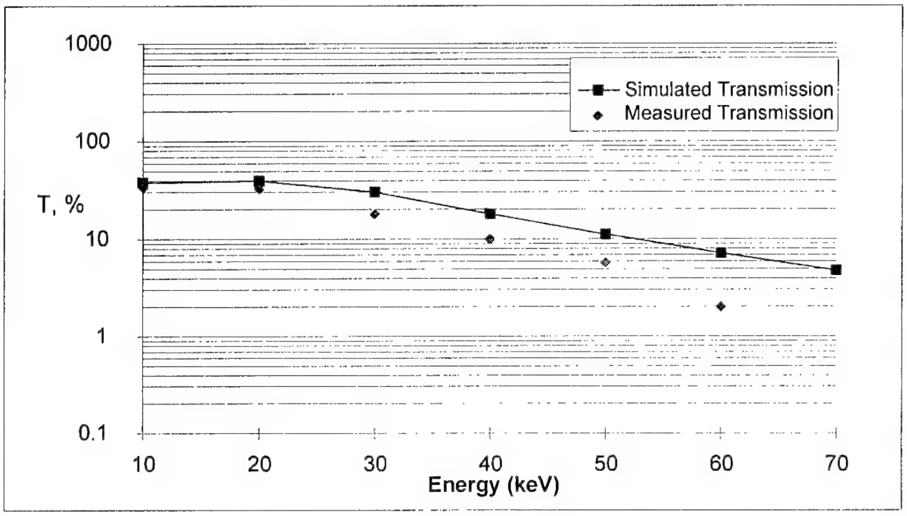

Figure 41. Simulated and measured transmission of the 20 keV prototype.

shown in figure 16. Waviness of the channels changes the divergence of the x rays exiting from the center of the lens from about 2.4 mrad to 4.0 mrad.

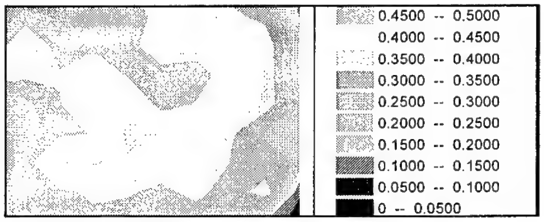

Figure 43. *Output intensity distributions for the prototype 20 keV collimator.*

6.3.1.2.3. 20 KeV prototypes

6.3.1.2.3.1. 1 m focal length optic

A second collimating lens designed for higher energies was also tested. This lens has a focal length, 1m, which was longer than ideal for mammography, but a much larger transmission, in excess of 30% at 20 keV, as shown in Figure 41. The drop-off at higher photon energies is due to some curvature of even the central fibers, and waviness of the internal channel walls. Waviness can cause a reduction of about 40 % on the overall transmission efficiency of the collimating optic at 20 keV. [20]The output field was also much more uniform than for the previous collimator, as shown by the picture in Figure 45 and the measurement of Figure 43. . At lower exposure, in Figure 44, it can be seen that there were some defects in the right half of the lens. This was due to some fiber misalignment, which was reflected in the divergence measurements. This lens was a first test of a new screen technology, which has since been improved.

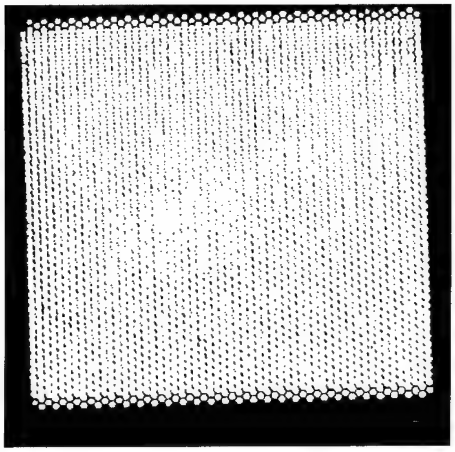

Figure 45. X-ray micrograph of 20 keV collimator, exposed 5 min at 60 keV and 0.4 mA with a W source and Polaroid film.

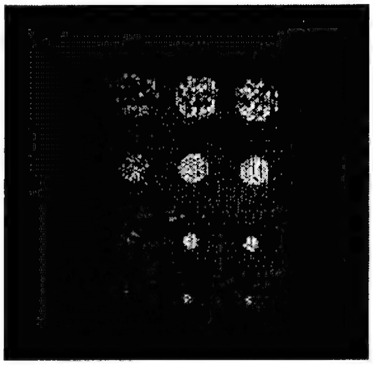

Figure 42. *Polaroid film radiograph of Lucite phantom placed 5 cm from the phantom. Upper holes are 6 mm in diameter, second row is 4 mm, third, 2 mm, and fourth, 1 mm. Holes on the right are 3.5 cm deep, middle holes are 3 cm deep and holes on left are 2 cm deep*

Preliminary imaging measurements have been performed with the optic. Figure 42 and Figure 46 are radiographs of a 5 cm thick Lucite phantom. Figure 42 was taken with the film 5 cm from the phantom. Figure 46 was taken with the film 95 cm from the phantom. There is no magnification

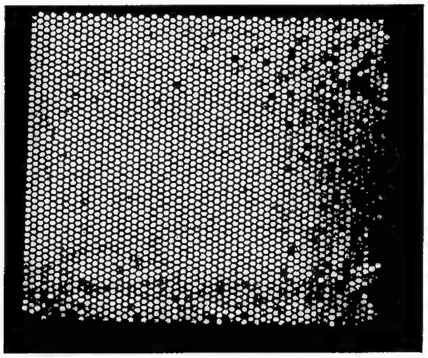

Figure 44. *X-ray photograph of 20 keV collimator, exposed 5 min at 35 keV and 0.25* mA..

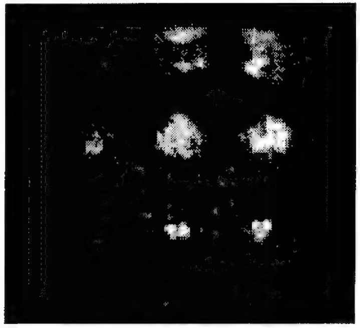

Figure 46. *Polaroid film radiograph 95 cm from the phantom.*

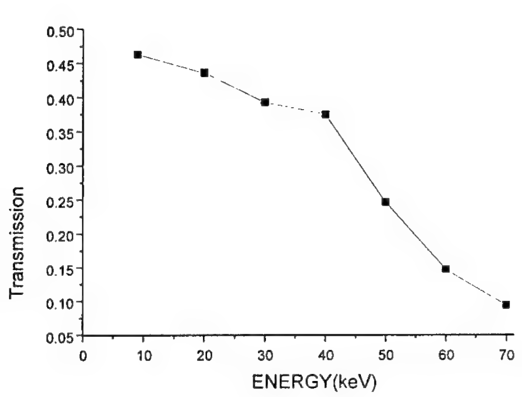

Figure 47. Measured transmission as a function of photon energy for 2 m focal length collimating lens.

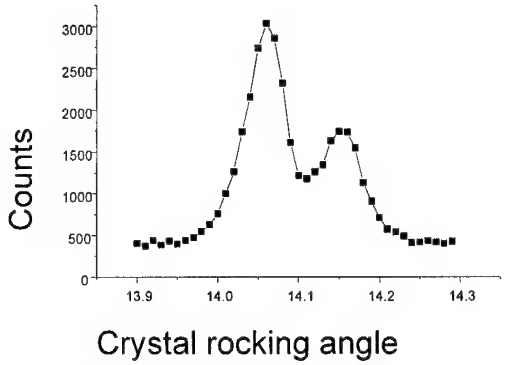

Figure 48. Output divergence of the 2 m focal length collimator, measured by rocking a silicon crystal in the beam. The Cu K alpha doublet is well separated, indicating a divergence of less than 4 mrad.

for this parallel beam geometry. However, some blurring due to fiber misalignment is observable. Given the long distance, known fiber misalignment and very low exposure the image is reasonably clear. The images were taken with normal, x-ray insensitive Polaroid film and a very low power, 0.20 mA test source. In both cases the phantom was placed close to the output of the lens.

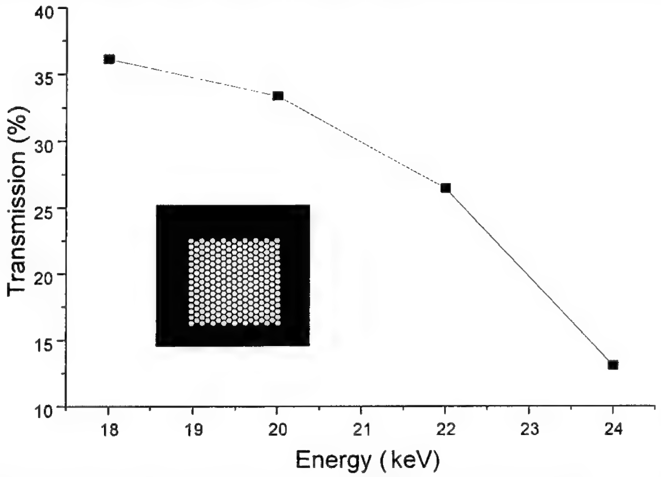

Figure 49 Transmission of the short focal length 20 keV prototype. *Inset is output x-ray image.*

6.3.1.2.3.2. 2 m focal length optic

An even longer focal length lens, while it has a smaller collection angle, has even better transmission, as shown in Figure 47. This lens had a transmission in excess of 40% at 20 keV, and very good fiber alignment, as determined from input focal spot size and output divergence measurements, as shown in Figure 48.

6.3.1.2.3.3. 24 cm focal length optic

A more appropriately designed collimating optic, with a focal length of only 24 cm, was produced. This optic has a 2.5° collection angle, a transmission in excess of 30% at 20 keV, and good uniformity, as shown in figure 49 .

6.3.1.3. ANTI-SCATTER OPTICS

6.3.1.3.1. Straight MultiFiber Optic

Rather than simply using long air gaps to eliminate scatter, a straight polycapillary antiscatter optic could be employed, as shown in Figure 24. Such an anti-scatter optic, which was essentially a 3 cm diameter bundle of straight polycapillary fibers, was aligned to the output of the 8 keV collimating lens. The anti - scatter optic was 150 mm in length with 55μm channels. The transmission spectrum of this optic is

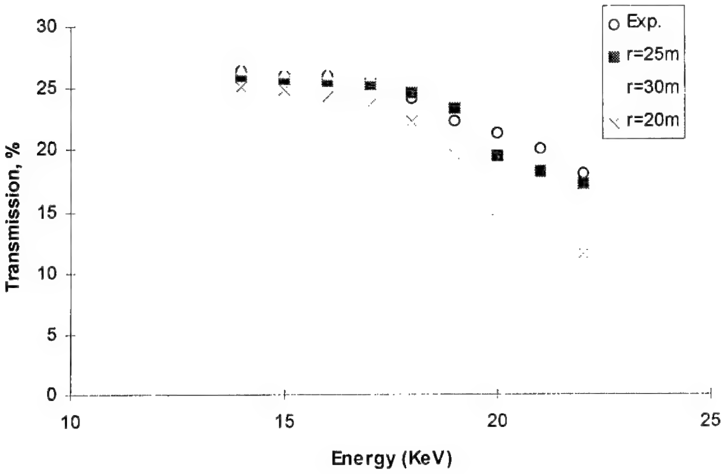

Figure 51. Simulation of straight antiscatter lens, compared to measured data. Simulation uses 1 nm roughness, 0.45 mrad waviness, and 26% overall open area.

shown in Figure 51. Simulations show that the apparently straight fibers have significant curvature, with radius of curvature of about 25 m.

6.3.1.3.2. Magnifying Linear Monolithic Optics

6.3.1.3.2.1. Transmission

Linear monolithic optics taper as a single glass unit from input to output as shown in Figure 2 and Figure 56. These optics are relatively difficult to manufacture. Many early prototypes have poor transmission, as shown in Figure 52. To help understand the defect problem an extensive simulation and measurement study was performed on several of the prototypes.

The focal distance of a polycapillary optic can be determined by finding the smallest scan angle or the maximum transmission. Source scan curves in both x (horizontal) and y (vertical) directions were recorded after the source and the lens were in alignment. FWHM of the scan curves in both directions are calculated with Gaussian fitting, and the average FWHM is taken as the scan width at that position.

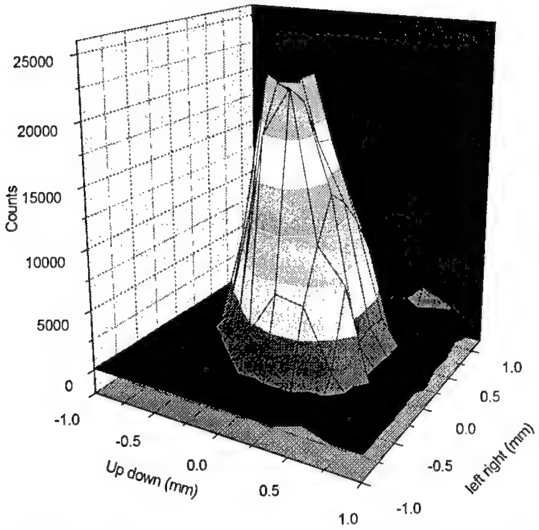

Figure 52. 2-D source scan of early prototype optic (input diameter = 2 mm, output diameter = 3 mm, transmission = 5 % at 20 keV, focal distance 22 cm) This lens transmits poorly because only the central capillary channels transmit while the outer capillaries do not transmit at all. Only about 33 % of the optic cross section transmits at 5 % or greater.

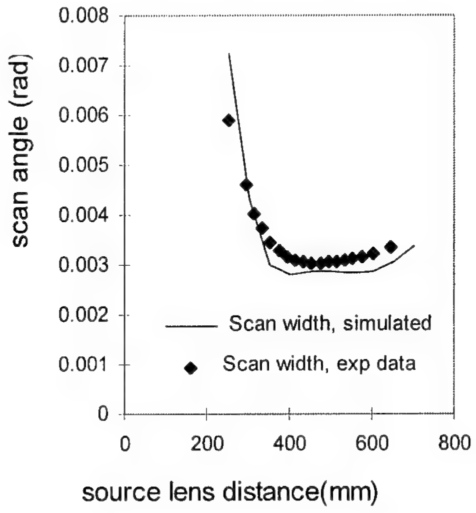

Figure 50. Source scan of tapered lens.

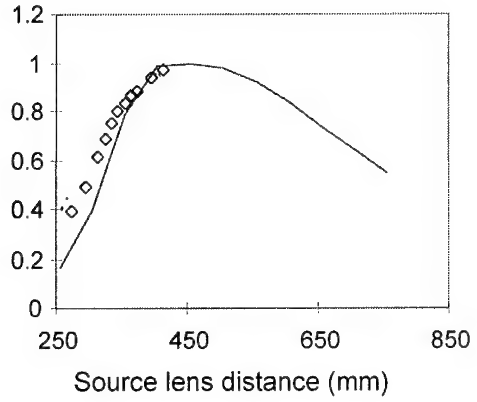

Figure 53. Transmission of tapered lens. Solid line is simulation.

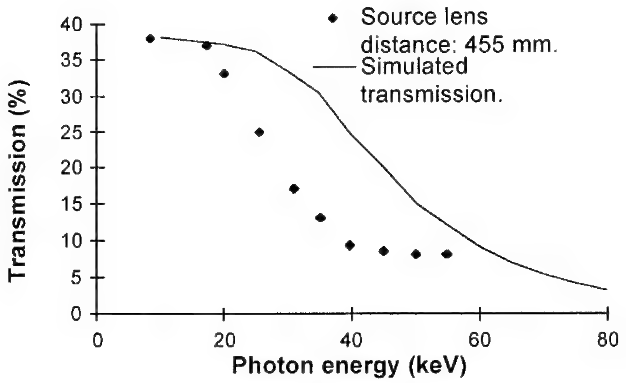

Figure 54. Transmission of whole tapered lens.

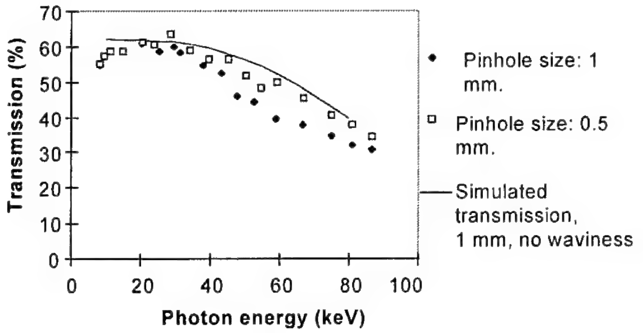

Figure 55. Transmission of the central part of the tapered optic.

Scan angle is defined as the result of the average scan width divided by the source-lens distance. In Figure 50, scan angle is plotted as a function of source lens distance. Since the theoretical curve does not have as many data points as the experimental curve, it is not as smooth as the experimental curve. This method is not affected by the source instability, and hence is very useful when the experiment needs a long time, and the source is not stable. However the curve is quite flat near the focal distance, as expected by simulation. The scan widths have to be measured very carefully to determine the focal distance. The focal distance determined by minimizing the scan angle is 455 mm for this lens. Transmission and photon counts are also plotted versus source lens distance in Figure 53 along with the simulation values. The maximum point for transmission is around 450 mm. The second method can be affected by the source instability.

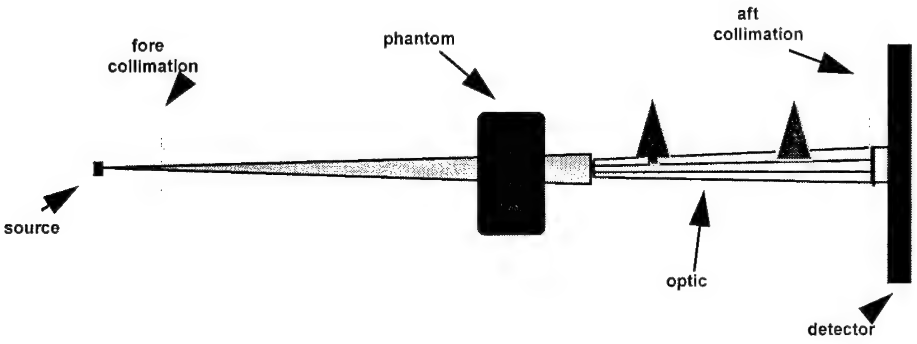

Figure 56. Small optic scanning geometry for contrast and imaging measurements.

Transmission was measured in a wide energy range for the whole lens as well as the central part of the lens. The transmission spectrum for the whole lens is plotted in Figure 54. The figure shows that the

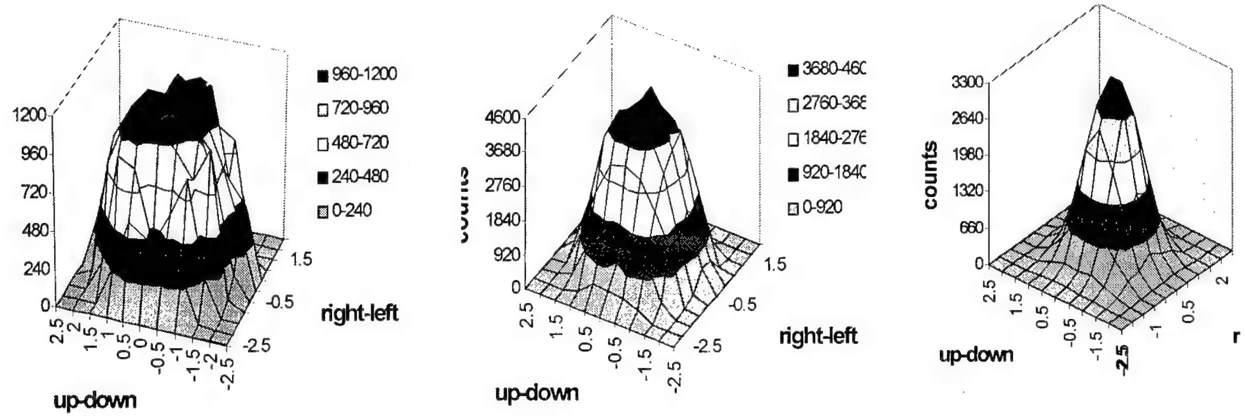

Figure 57. Two dimensional scans of the output of the tapered optic.

transmission drops quickly for photons with energy higher than 20 keV, but the transmission under 20 keV is almost flat. The low transmission in the high energy range can be explained by the non-linearity of the lens. The outermost channels are more bent than the central channels, so they have low or zero transmission at the higher photon energies. This is confirmed by the higher transmission measurement at the central part of the lens, shown in Figure 55 and the transmission uniformity measurement at different energies, shown in Figure 57. Transmission uniformity of the lens was measured by putting a 200 μm pinhole in front of the lens and performing a two dimensional scan. At 8 keV, the whole lens transmits, although we can see the transmission is not completely flat due to the non-linearity and the defects of the lens, such as blocked channels. At 25 keV, transmission of the whole lens drops to 25%. Most of the lens is still transmitting at 25 keV, but the outer channels have lower transmission than the central part. At 35 keV, the lens has a narrower transmitting region. The measurements show that the lens has undesirable nonlinearity.

6.3.1.3.2.2. Defect Study

Studies were performed on another optic to investigate the distributions of defects which diminish transmission. A poorly transmitting optic was cut into two pieces. The transmission of the pieces compared to the original is shown in Figure 61. The x-ray image produced by the two pieces is shown in Figure 59. The final piece, A, was cut into three pieces, A1, which was 11 cm long, and A21 and A22, which were both 5.5 cm long. The defect localization into A21 is shown by the image of Figure 58 and the transmission measurement of Figure 60. The transmission of the defected piece is higher at 24 keV than at 20 keV,

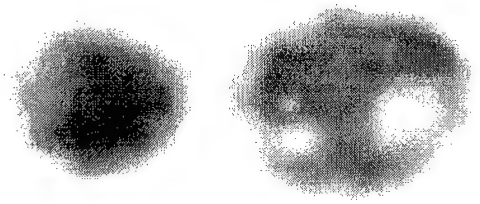

Figure 59 X-ray micrograph of pieces B (left) and A (right). A is larger since it is toward the large end of the taper, and contains the defect.

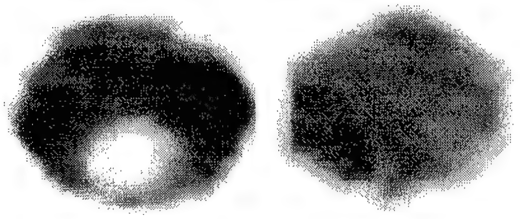

Figure 58. X-ray micrograph of next-to-last and last 5.5 cm of the optic (pieces A21, left and A22, right). A21 has a defect.

which is the reverse of what is expected from the variation of critical angle with energy. The transmission dip could be due to glass blockages in the channels, which would be more transparent at higher energies. The competition between the increasing penetration of the blockages and the decreasing channel transmission with increasing energy produces a transmission minimum, as shown in Figure 60.

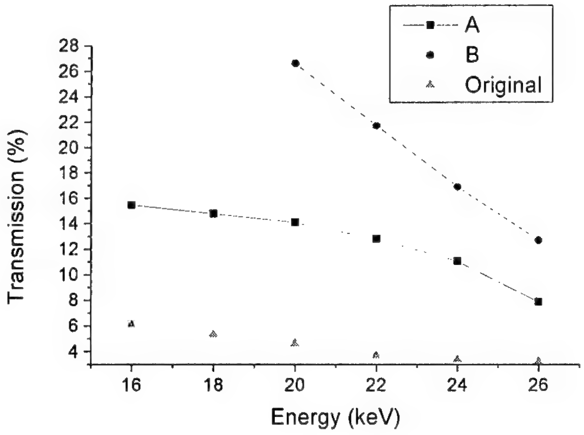

Figure 61. Transmission of original optic compared to two pieces. B is the first 10 cm (closest to the source), A is the final 22 cm.

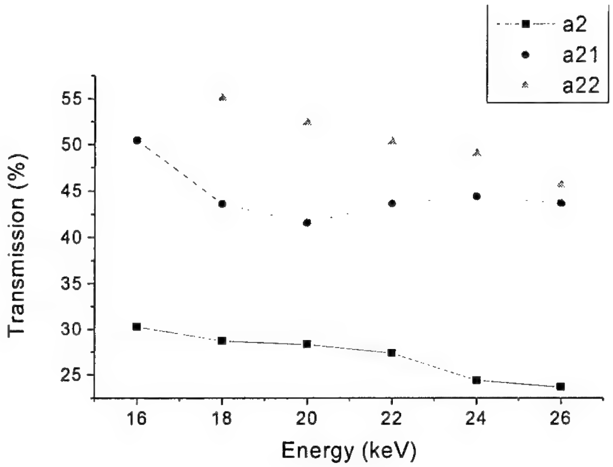

Figure 60. Transmission of final half of A (A2), and its two constituent pieces, the first 5.5 cm, A21 and the final 5.5 cm, A22. A21 contains a defect.

6.3.1.3.2.3. Simulations

Modeling defects, including waviness, bending, and blockages, require sophisticated simulations. The simulations plotted in Figure 53 and Figure 54 used the same roughness and waviness correction as that used for fiber D in Figure 5. A linear tapered lens is ideal for mammography, because, as shown above, any curvature can cause transmission reductions. However, the lenses currently available have nonlinear profiles. The profile is not circular, but to simplify the simulation, we assume that the profile is circular. A uniform bending will provide the best transmission performance for a given bending angle, so the simulation will overestimate the lens performance. A further simplification assumes the lens has a fixed channel size, although the channels actually taper with the lens.

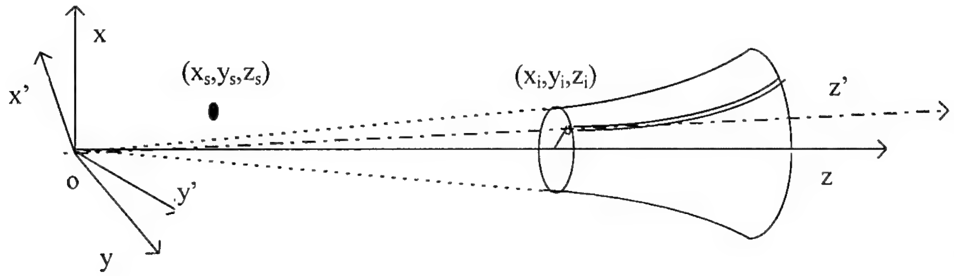

Figure 62. Geometry for Lens simulation.

The geometry for uniformly bent nonlinear lenses is shown in Figure 62. The simulation method for a uniformly bent lens is an extension of

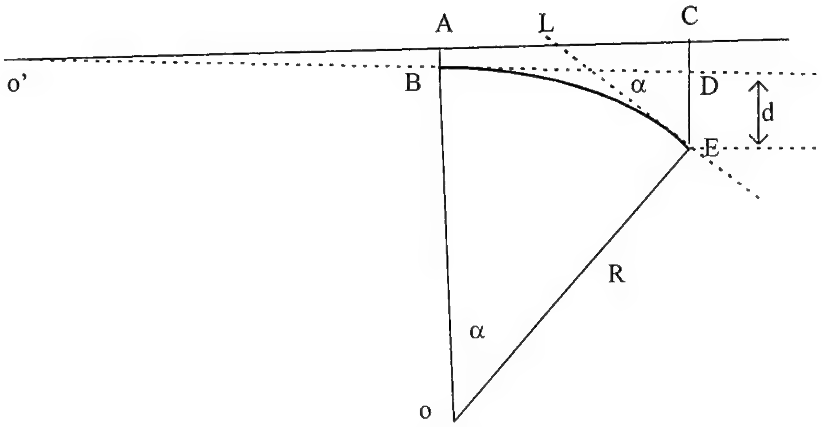

Figure 63. Curvature estimation for lens simulation.

the simulation for uniformly bent polycapillary fibers. The simulation is done by sampling channels in the input cross section of the lens with an even step size. In the simulation for a bent fiber it is assumed that the capillary bends in -y direction, and z direction is along the input axis of the fiber In order to reuse the old simulation code, the coordinate of the simulation x-y-z is rotated to x'-y'-z', where z' is the direction of channel axis at the input end and -y' is the channel bending direction. Assuming the source position and the capillary position at input end is (x_s', y_s', z_s') and (0, 0, z_i') respectively, then the source capillary distance is $z_i' - z_s'$. The origin of the coordinate is selected to be the focus point of the lens.

Another parameter needed by the simulation is the bending curvature of the selected channel. This value varies with the position of the channel. The calculation of the bending curvature is demonstrated in Figure 63.

First it is assumed that the channels are evenly distributed on both input and output cross section. Let input and output diameter of the lens be r_i and r_o, and focal distance $\overline{O'A}$ be f, and the lens length $\overline{AC}$ be L, then

$$\overline{AB} = \sqrt{x_i^2 + y_i^2}, \quad \overline{CE} = \overline{AB} * r_o / r_i$$

$$f / (f + L) = \overline{AB} / \overline{CD}, \quad d = \overline{CE} - \overline{CD}$$

For a small bending angle,

$$\alpha \approx L / R = d / (L / 2)$$

where R is the bending radius, d is the distance between point D and E as shown in Figure 63, and α is the bending angle. Thus

$$R = L^2 / 2d \qquad (11)$$

The simulated results in Figure 54 and Figure 55 show higher transmission than the experimental results. This indicates that the lens has more reduction in transmission due to the bending. This is expected, because the lens does not have a uniform bending.

6.3.1.3.2.4. Potential for Lead Glass

Transmission from early fibers was poor in the whole energy range. Recent fibers are more promising. Transmission for an early 95 mm long and a more recent 125 mm long lead glass polycapillary fiber is shown in Figure 64. The transmission drop at lower energies may be caused by partially blocked channels. Transmission can also be improved by using a short optic. Almost total scatter rejection is expected for a lead glass optic longer than 30 mm.

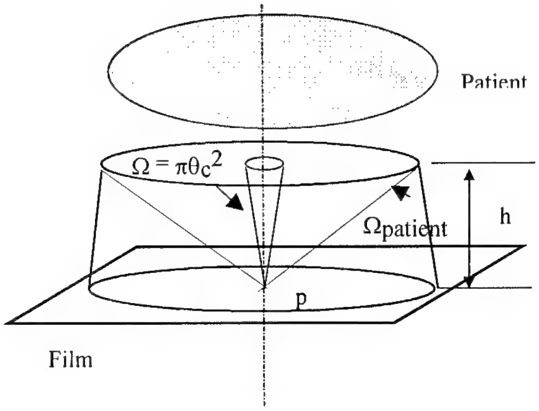

Figure 65. An ideal large area lens.

6.3.1.3.2.4.1. Calculation of Contrast Improvement and Relative SNR

Lenses with large diameters are not currently available. Their potential behavior can be predicted by scaling up existing measurements to a large area lens, as shown in Figure 65. The value of h is the length of the optic. For a point *P* on the film, scattered radiation could come from any direction in the solid angle $\Omega_{patient}$, which is the solid angle subtended by the patient. The transmission for scattered x rays can be calculated from equation (9). The calculated scatter transmission depends on the length of the photon path through the optic. Making a very conservative estimation, we can fix this length to the length of the optic. There is also a small part of the scattered x rays that have almost the same direction as those primary x rays. This part of the scattered x rays with an incident angle less than critical angle could still pass through the channel. So the total scatter transmission of the lens is

$$T_{s-optic} = \frac{N_{s-optic}}{N_s} = T_s + \frac{T_p \cdot \pi\theta_c^2}{\Omega_{patient}}, \qquad (12)$$

where $N_{s\text{-}optic}$ is the number of scattered x rays with the optic, N_s is the number of scattered x rays without the optic, T_s is the transmission for large angle scattered x rays, T_p is the transmission for primary x rays, $\Omega_{patient}$ is the angle subtended by the patient, θ_c is the critical angle for transmission in the channels. Because the critical angle is on the order of 10^{-3} radians, the second term is very small, and can be ignored. So scatter transmission of the lens can be estimated to be equal to large angle scatter transmission, T_s, which can be calculated from equation (9), and nearly scatter free lenses can be obtained by using a suitable length optic. In the above equation, we assumed that the angular distribution of the scattered x rays is isotropic. If the scatter distribution is not isotropic, the second term in equation (12) can be larger than expected, but will still be very small, and this assumption will not significantly effect the result. In equation (12), T_s ,

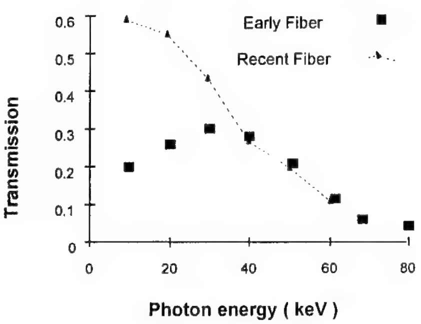

Figure 64. Transmission as a function of photon energy for a lead glass capillary. The fibers are 105-120 mm in length.

T_p and θ_c are all energy dependent. In the case where x rays with a wide x-ray spectrum are used, T_s and T_p should be replaced by the average large angle transmission and primary transmission. To avoid underestimating scatter transmission, θ_c can be set to be the critical angle for the lowest energy in the spectrum.

Table III. Transmissions for three lenses. The results for the ideal borosilicate lens are measured results for the center part of the prototype lens. The results for lead glass lens are simulated with 120 kVp spectrum and a W target.

Lens #	Lens type	Length (mm)	Photon Energy	Primary transmission $T_{p\text{-optic}}$	Scatter transmission $T_{s\text{-optic}}$
1	Ideal borosilicate Lens. Scaled up from the center part of the prototype lens	166	20 KeV	0.6	0.0
			45 KeV	0.55	0.002
			60 KeV	0.55	0.005
			70 KeV	0.45	0.03
2	Actual Borosilicate prototype lens	166	20 KeV	0.33	0.0
3	Lead glass	30	69 KeV	0.63	0.0076

The scatter and primary transmission of the optic determine the performance of the capillary lens. For example, if the scatter fraction before the capillary lens is F, then the scatter fraction after the lens, F_{optic}, is

$$F_{optic} = \frac{F \cdot T_{s-optic}}{F \cdot T_{s-optic} + (1-F) \cdot T_{p-optic}} = \frac{KF}{1-F(1-K)}, \qquad (13)$$

where $T_{p\text{-optic}}$ is the primary transmission of the lens and K is the ratio

$$K = \frac{T_{s-optic}}{T_{p-optic}}. \qquad (14)$$

The contrast enhancement achieved by using the optics is

$$\frac{C_{optic}}{C_{no-optic}} = \frac{1-F_{optic}}{1-F} = \frac{1}{FK + (1-F)}. \qquad (15)$$

The contrast enhancement alone is not the only relevant quality factor. The signal to noise ratio (SNR) is another important quality factor. According to the Rose model,

$$k^2 = C^2 \Phi A, \qquad (16)$$

where k is the SNR, C is the contrast, Φ is the photon flux, and A is the area of the target. In order to compare the SNR for different scatter rejection devices, relative SNR was used. Relative SNR is the SNR normalized by the SNR without any scatter rejection device,

$$k_r^{\,2} = \frac{k^2}{k_0^{\,2}} = \frac{C^2}{C_0^{\,2}}(FT_s + (1-F)T_p), \qquad (17)$$

where k_r is the relative SNR. C and C_0 are the contrast with and without out the scatter rejection device, respectively. T_s is the scatter transmission and T_p is the primary transmission of the device.

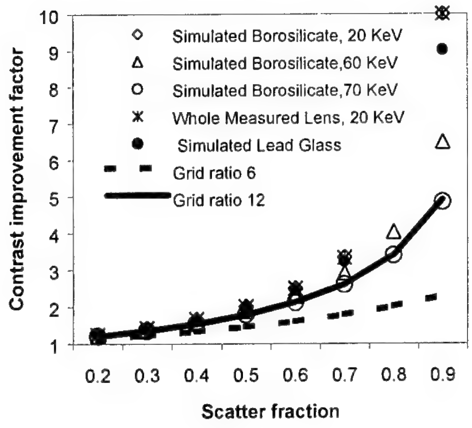

Figure 66. Contrast improvement vs. scatter fraction for the three lenses. The results were compared with the performance of two commercial grids.

6.3.1.3.2.4.2. Performance of Three Hypothetical Lenses

Performance estimates of three hypothetical lenses are given in Table III. The ideal borosilicate lens is scaled up from the center part of the measured lens. Simulated transmission was used for the lead glass lens. The absorption of the lenses are given by equation (9). The performance of the three lenses was compared with the performance of the conventional grids described in *Table IV*. The primary and scattered transmissions of the different grids in *Table IV* were measured at 69 keV, which is the average energy of the 120 kVp tungsten spectrum, and with scatter fraction of 85%, by C. E. Dick and J. W. Motz [21]. It is assumed that the scatter and primary transmission are the same under different scatter fraction. This assumption is correct if the angular distribution of the scattered x rays does not change. The performance of the grids is assumed to be energy independent. They might perform better at lower photon energies if the scatter transmission is due to the lead plates which are not thick enough to absorb the incident x rays. However, it was assumed the dominant mechanism for scatter transmission was x rays passing through the interstitial material. The contrast enhancement and relative SNR were calculated under different scatter fractions and plotted in Figure 66 and Figure 67.

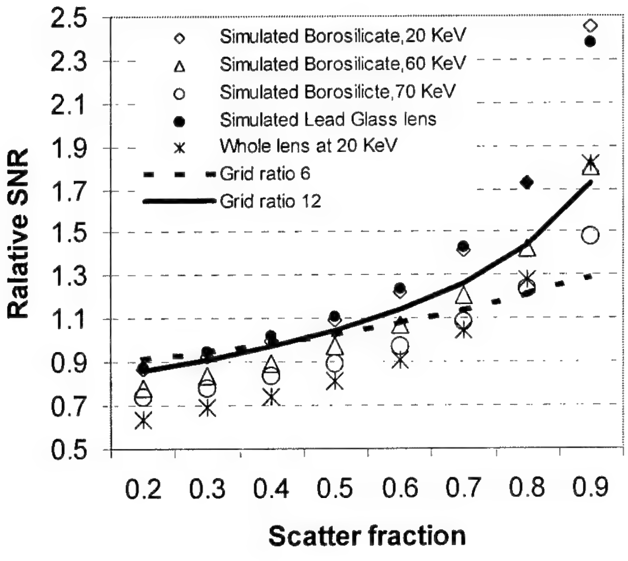

Figure 67 Relative Signal to Noise(SNR) vs. scatter fraction for three hypothetical lenses. The results were compared with the performance of three commercial grids.

For most medical x-ray imaging applications, the effective energy ranges from 20 to 70 keV. Mammography has an effective energy of 20 keV. The results in Figure 66 show that contrast improvement of all the three hypothetical lenses are better than or as good as that of the three grids. Lens #2 is scaled up from the whole measured lens. This lens has good contrast improvement because of its total scatter rejection. However its relative SNR is lower than that of the grids when the scatter fraction is less than 80% because of its low primary transmission. The primary transmission of this lens is only 33% and the primary transmissions for all the three commercial grids are better than 60%. So with this lens more exposure will be necessary to the patient. Overall primary transmission has to be improved for practical use. Lens#1 is scaled up from the center part of the measured lens. From the calculations, summarized in Figure 66 and Figure 67, its performance is significantly better than those of the commercial grids for effective energies of 20-45 keV. This lens will not only improve the contrast in the imaging but also reduce the exposure time to the patient. So it is ideal for mammography.

Assuming that the lead glass capillaries have the same quality as that of borosilicate fibers, we can estimate the performance of a lead glass lens. Simulations of transmission spectra were performed for a source to lens distance of 1.5 m, and the source operated at 120 kVp with a 0.5 mm spot size. For a perfect lens, each channel in the lens is tapered. With a tapered channel, fewer average reflections will be needed for the photons to pass. So theoretically, transmission with a perfect lens is larger than for a straight capillary if they have the same quality. The transmission is quite sensitive to the capillary length. Therefore, as long as the lens has low enough scatter transmission, the length of the lens should be kept as short as possible. The performance estimation results of the lead glass lens in Figure 67 are based on the simulated transmission with length of 30 mm. The scatter transmission of this lens is less than 1%. Primary transmission as high as that of grid is also obtained with simulation. Compared to the grid performance, this lens has higher contrast enhancement and relative SNR. So this lens will not only improve the contrast of the image, but also reduce the radiation dose to the patient.

6.3.1.3.2.5. Manufacturing Issues

The only practical method to produce larger linear tapered anti scatter optics is to couple several smaller optics together to form one large optical component. The method we used to attach the individual optical elements together is quite similar to the method that is used by the company to align polycapillary fibers. These multifiber devices consist of thousands of individual polycapillary fibers that are strung through rigid grids to produce a single large optic. The individual fibers must be aligned to within a few microns in position and to less than a milliradian in angular orientation. These requirements are more stringent than those required in this project. The alignment technology is not likely to be a problem. However, first high quality monolithic tapers must be reproducibly manufactured.

There has been substantial progress in achieving the necessary manufacturing control to repeatably produce high quality optics. The manufacturing technique was carefully studied, the critical problems were identified, and a plan was prepared to modify the manufacturing process. The first step was to increase the controllability and reproducibility of the manufacturing process. The development of monitoring automation and feedback systems was achieved. As a result of the improvement in process control, systematic and rapid improvement has been made in the development and manufacturing of new optics.

Initially, glass preforms and prototype optics were produced in Russia. They were of relatively poor quality, and no two optics were equivalent in performance, but they served as proof-of-principle devices. Because of the technical and political difficulties, Russian optics and preforms are no longer available. When it became apparent that having the optics manufactured in Russia was not viable long term, X-Ray

Table 3

PROBLEMS	ACTION NECESSARY
• decrease in open area	• better temperature profile control • better tension control • evaluate tension - temperature trade off
• inclusions, primarily glass particles	• improved handling and bundle assembly procedures • static electricity abatement including controlling for humidity • laminar flow hoods
• cast (curvature)	• improved alignment of feed mechanism, furnace, and puller • radially symmetric uniformity of heat zone • longer cooling zone • better control of air flow
• OD control	• improved temperature and tension control • real time monitoring of OD with closed loop feedback
• waviness in glass surface	• elimination of internal vibration sources, e.g., friction, motors being operated slower than designed, turbulent forced air cooling • isolate from external vibration sources • change to cutter approach which doesn't cause large periodic shocks • more homogenous glass (optical quality)

Optical Systems, Inc. (XOS) commenced developing a U.S. manufacturing capability.

XOS chose to work with the polycapillary subcontractor that has the best controlled process for making polycapillaries which work well at 8 keV. The glass is formed by a continuous, steady state, vertical pulling process, with as much as 1,000 meters in a single production run. Several manufacturing runs were conducted with evaluations of the polycapillaries done between each run. Adjustments to the process were made for each new run. XOS personnel participated in some of the runs. The polycapillary performance and the manufacturing process were carefully analyzed to determine what changes were needed in manufacturing to obtain the desired polycapillary capabilities. This manufacturer does not use computer control. There was no automatic feedback in the manufacturing system. The system was controlled by having an operator observe that a condition such as the outer diameter of the polycapillary or the furnace temperature had drifted from the desired point and then manually adjusting one of the control variables. The polycapillary performance at high energies was not acceptable. Problems which were identified, and the actions determined to be necessary are identified in the Table 3. XOS determined that this supplier was not able and/or willing to make the necessary equipment, personnel, and operational changes. With this information, XOS modified an in-house glass pulling system to investigate the effect of making some of the changes which were determined to be necessary.

A systematic evaluation the major manufacturing parameters was not possible initially as the first prototypes made were pulled on a setup where there was little control over the manufacturing parameters, and little ability to record the parameters during the forming process. The initial setup was put together inexpensively to provide some indication of the direction to proceed. It enabled a definition of a general range for some of the manufacturing parameters, such as pulling speed, so that acquired information could be used to design a more sophisticated pulling setup. One source of variation in the prototype monolithic optics came from the uncontrolled air flow through the furnace.

Modeling of the optic shaping process was conducted. Modeling provides some understanding of the underlying relationships between the manufacturing parameters and the resulting optic. Constant feedback of the experimental results to increase the accuracy of the model is an important input to the scientific, quality, and production methods. The modeling is based on a one-dimensional finite-differences algorithm. The preform (large outside diameter polycapillary bundle) is split into finite elements. This approach allows the thermal and mechanical properties of each segment to be calculated. At each time step, the ends of the preform are moved according to a predetermined, but likely variable, speed. The formation of the lens occurs in the heated area and the glass will flow according to viscosities. Since the total volume of each element is kept the same, the elements that are stretched the most end up with the smallest diameter. The radiative heating by the furnace as well as radiative cooling from the preform must be considered. The thermal profile for the preform can be calculated for points along the center axis of the furnace.

A second generation pulling tower was constructed and instrumented to allow flexibility in controlling different parameters and to record the actual status of parameters during the pulling. The tower uses servo motors with encoders to displace the preform and furnace; multiple thermocouples to monitor the temperatures; and load cells to monitor the pulling forces. There are numerous independent and dependent variables that effect the quality and reproducibility of a lens design. The preform material was characterized for open area, x-ray transmission, uniformity of outside

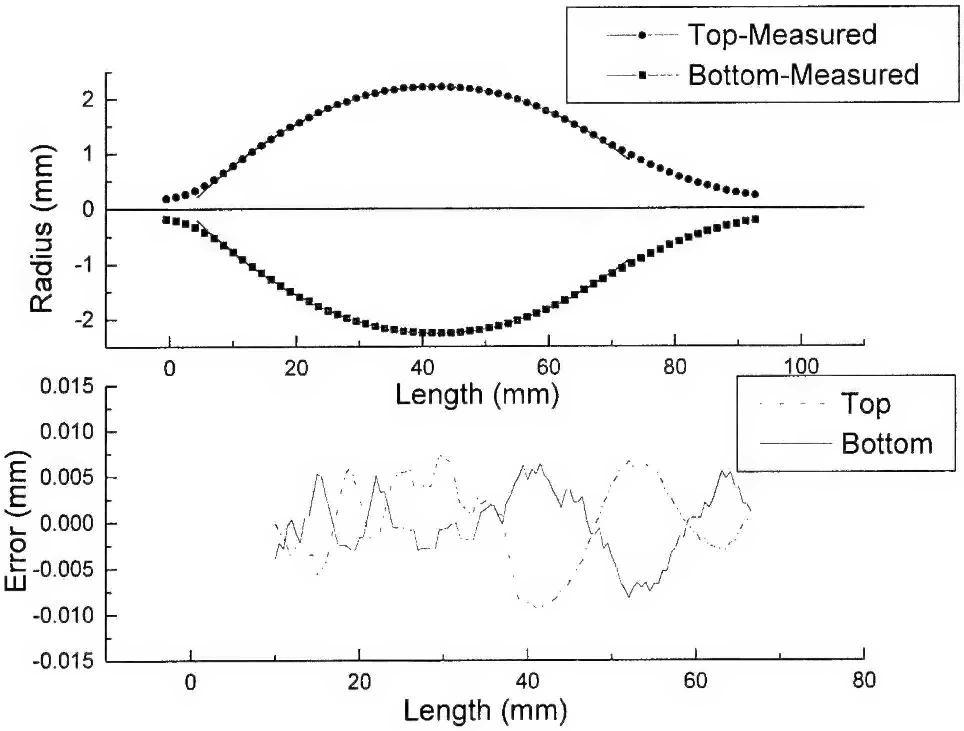

Figure 68. Variation in optic profile, compared to design.

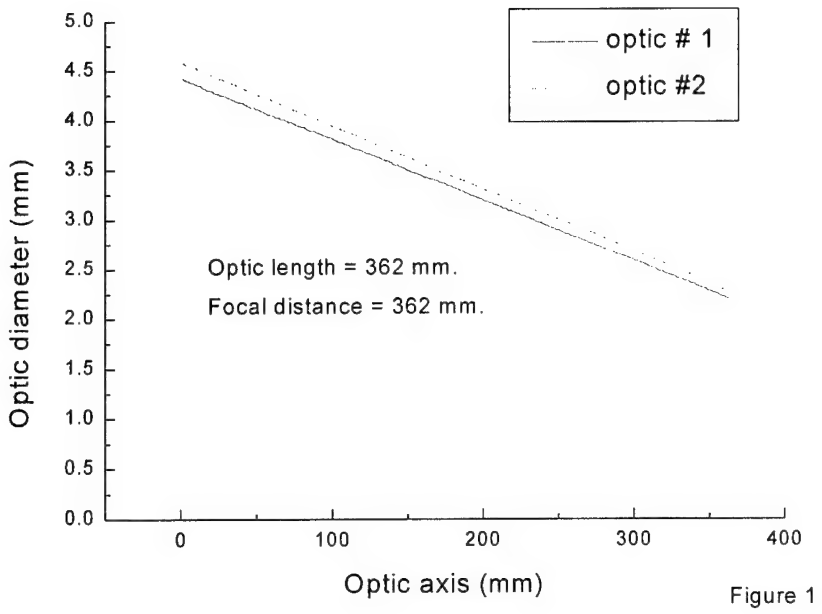

Figure 69. Profiles of two recently manufactured matched linear tapers.

diameter. Precautions to protect the material from dust and moisture were taken.

There is a strong interdependence of tension on the preform, temperature in the various heating zones, speed of the pull, and mechanical feedback. Extensive correlation of the data from the forming process with the lens performance was needed to optimize the system. Additional considerations include the heat capacity of the glass and time-temperature response of the furnace. Uniformity of gas flow through and around the glass during the pulling step is important to monitor. To assure uniformity and appropriate use of heat zones, other parameters to consider include: baffling, furnace diameter, and correlation of furnace motion with the movement (i.e. flow) of the preform. In a motor driven system, there are vibrations, motor inertia, slew rates, as well as bearing, slide, and belt qualities that must be evaluated. Other mechanical conditions to evaluate include how the preforms are held and supported to maintain uniform alignment and minimize random and systematic perturbations. Despite the number of parameters to be considered, only a few are thought to be critical to first order, others affect the quality in diminishing amounts. In fact, most do not become an issue of concern until the grosser variable are better controlled. Fairly early in the process, XOS made significant progress in the design and construction of monolithic polycapillary optics.

The first example is a set of 17 keV focusing optics designed for microfluorescence analysis. The profile of the optic was measured with a microscope-based MicroVu video coordinate measuring system at XOS. The precision of the system is about 5 μm. Figure 68 shows the measured profile compared with the design profile. Deviations along the optic axis between the two profiles are also shown in Figure 68. Two very well matched magnifying linear tapers were produced for placing in a multi-taper jig. The profiles of the two optics are shown in Figure 69. Although the optic profiles are excellent, x-ray transmission efficiencies of the first four optics fabricated were pretty bad (less than 10%). Based on x-ray characterization on both original bundles and long linear tapers, we concluded that the poor x-ray transmission is due to randomly distributed defects in the original bundles. With the improvements in measurement capability and the lens shaping tower improvements, which include improved control and feedback, XOS is in a position to produce tapers with improved

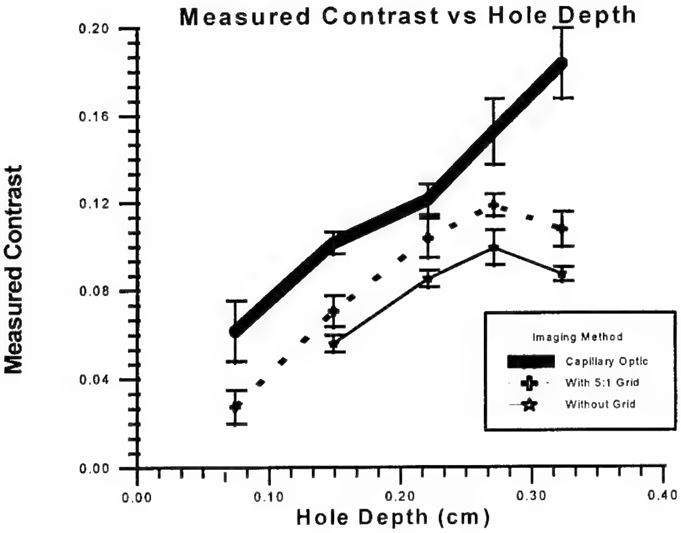

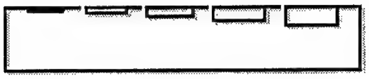

Figure 72. Contrast enhancement measured for a small scanned capillary optics using a phantom consisting of a Lucite block with drilled holes.

profile. Problems with poor optic transmission and inconsistent quality form the current glass preform supplier have been substantially reduced. Further, XOS has brought on-line the capability to produce polycapillary preforms in house.

6.3.1.3.2.6. Imaging Measurements

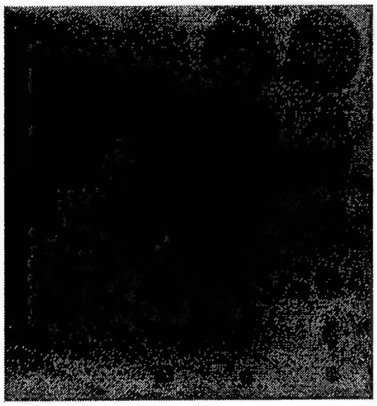

Figure 71. Image of contrast phantom made with scanned optic.

Figure 70. Image of contrast phantom produced with conventional grid.

Contrast enhancement measurements have been performed with a small scale (2 mm diameter) optic at the Univ. of Wisconsin.[22] The geometry for the scan is shown in Figure 56, and the resulting contrast enhancement compared to the no optic and conventional grid cases are shown in Figure 72. An image made with a scanned optic and with a conventional grid are shown in Figure 71 and Figure 70. Improvements have been made in the scanning system to reduce image artifacts. Scan lines which were visible in previous images are not apparent in Figure 71.

The optic was also used to measure the resolution enhancement due to magnification. A plot of the measured MTF is shown in Figure 75. At the 0.1 MTF

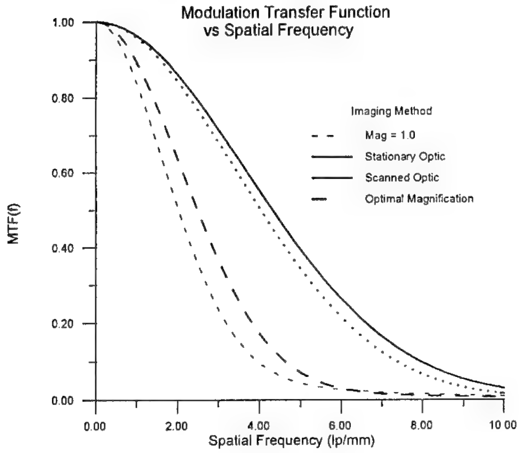

Figure 75. Modulation transfer function.

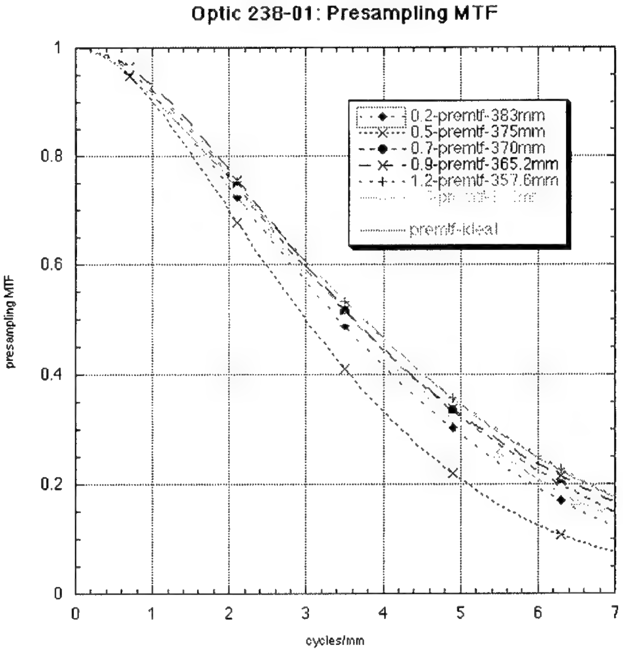

Figure 73. MTF of newest, most linear taper at different source to optic distances. MTF is nearly ideal.

level, the resolution improved from 4.5 lp/mm^2 without the optic to 8.9 lp/mm^2 with the optic. The MTF of the very linear optic from Figure 69 is shown in Figure 73. It shows nearly ideal performance despite the low transmission.

Magnification with the optic actually can occur before, in the optic and after the optic. Using some geometric magnification before and after the optic may permit larger oveall magnification or may permit a shorter optic to be used while still maintaining adequate magnification. Preliminary calculations show that for an optic with a magnification of 2.0, overall magnification of 2.25 may be acheiveable.

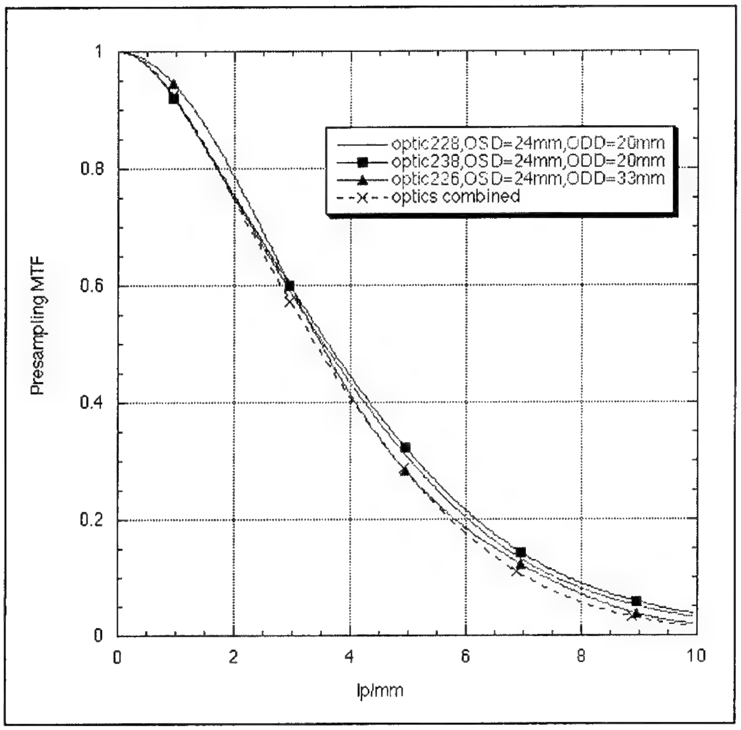

Figure 74. MTF of multiple taper optic and the three individual optic components..

Finally, to improve the speed and accessibility of MTF measurements, a technique employing a standard slit camera has been developed.[23]

6.3.1.3.3. Multitaper Optic

Three tapers were assembled into a "multitaper" optic. Alignment of the tapers on the first prototype grid was to within 1.7 mrad, not quite optimal. However, the MTF, as shown in Figure 74, was nearly as good as for the individual tapers.

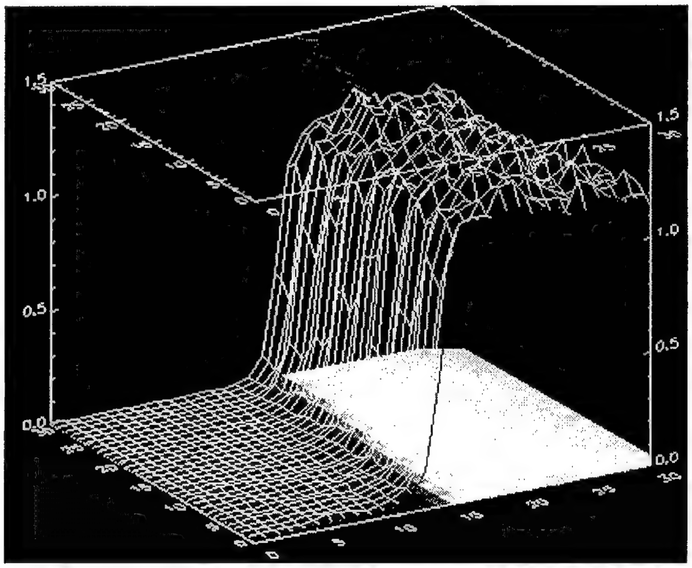

Figure 78 Three-dimensional edge image after background subtraction.

6.3.1.4. ARTIFACT REDUCTION

Modulation Transfer Function (MTF) is the most fundamental measurement of spatial resolution used in radiology. The standard technique is to image a slit, determine the line spread function (LSF), and compute the Fourier transform. The MTF measured for the mammography system with capillary optics, compared to that without the capillary optics, will give the resolution improvement and also can be used to diagnose artifacts. For some lenses, the transmission is not always uniform, as shown in figure 62, which is an image of the output from a lens.

The structure of the capillary bundles was obvious. In this case, the LSF could not be obtained by imaging a slit without background elimination. The background deducted slit image is the slit image divided by the image with capillary only. However, this involves image registration. The information for background that can be used for image registration is too little in the slit image. An alternative method is calculating the LSF as the derivation of the edge spread function (ESF). The edge image left enough background for registration so that it could be a feasible method in our case.

A registration algorithm (FMI-SPOMF) proposed by Chen, et al. [24] was used in this work. This is a method to match a two-dimensional image to a translated, rotated and scaled image. The approach consists two steps: the calculation of a Fourier-Mellin Invariant (FMI) descriptor for each image to be matched, and then matching of the FMI descriptors. FMI descriptors are translation invariant. The matching of the FMI descriptors is to find out the rotation and scaling, and achieved using a symmetric phase-

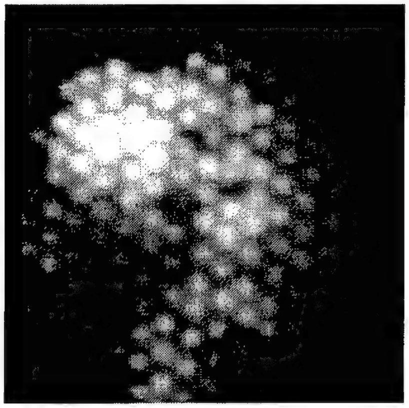

Figure 76. Magnified image of the background with lens structure. Real size: 5(mm) X 5(mm).

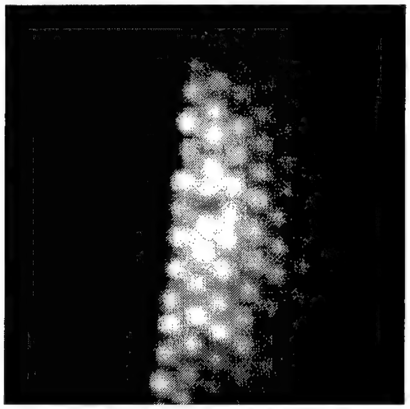

Figure 77. Magnified image of a lead edge. Real image size: 5(mm) X 5(mm).

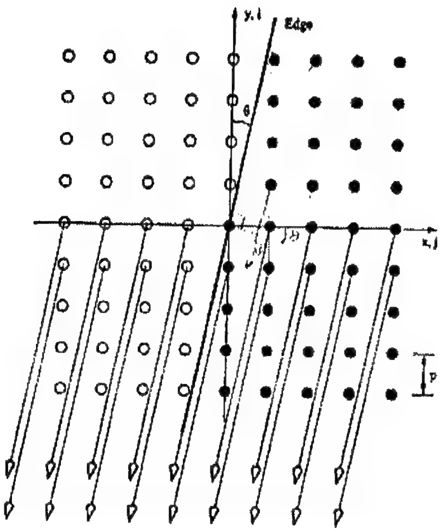

Figure 80. Reprojection of a two-dimensional edge image into a finely sampled ESF.

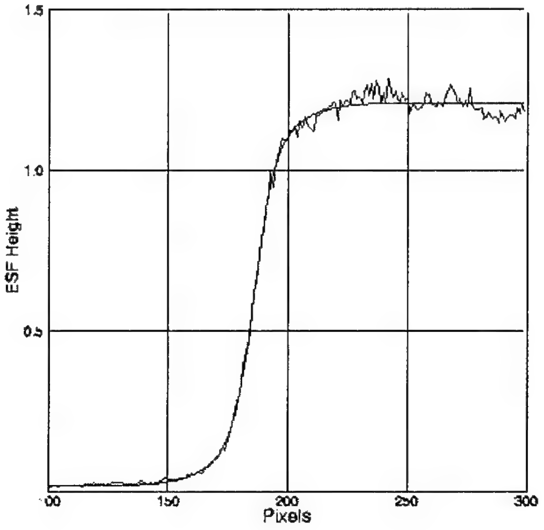

Figure 79 Edge spread function and its fitting curve.

only matched filtering (SPOMF). In our case, there is no change in scaling, but rotation is probably involved. When the rotation was found, image translation is found by SPOMF method.

Images with and without edge are shown in Figure 77 and Figure 76. The edge was made of a lead plate. The size of each image is fifty by fifty in pixels. They were taken in an experimental digital mammography system with a computed radiography digital phosphor plate. The digital CR plate has limited resolution, 5 lp/mm, and is usually considered to be not good enough for clinical mammography. But the effective resolution of the system could be improved by the magnification of the capillary optics. The magnification of the capillary lens used in the system is 1.86, so that the effective resolution should be improved by a factor of 1.86.

The registration algorithm was implemented in IDL. With the FMI-SPOMF registration algorithm, no rotation was found. The translation was then found by SPOMF algorithm. The difference between the usual correlation method and SPOMF method is that it only uses the phase information. The phase-only correlation function has sharper peak than normal correlation function. Sub-pixel resolution could be achieved theoretically. However it was found that the resolution is not good enough in our case. This may be caused by the relatively small image size. The background-subtracted result was further optimized by manual shifts in sub-pixel range. The result after manual optimization was shown in Figure 78 . The periodic background is totally gone. A cubic spline interpolation method was used for the best result while shifting the background image relative to the edge image.

The presampling MTF includes unsharpness of the detector and the sampling aperture. In order to eliminate the aliasing, a finely sampled ESF is obtained with a slightly angulated edge in a single exposure as illustrated in Figure 80.[25,26] The angle in our edge image in Figure 78 was calculated to be around 6 °. The resultant ESF is plotted in Figure 79 . A direct calculation of MTF is to take the derivation of the ESF and result a LSF, then take Fourier transform. As it can been seen, the ESF in our case is not smooth enough for a direct calculation. An alternative technique is to use an ESF fitting procedure.[27] In the fitting method, the ESF is represented with a term (1-exp) and an error function (erf) as in equation (18). MFT is calculated by equation (19), where a, b, c and d are fitting parameters from equation (18). The fitting curve is plotted in Figure 79 as the solid line.

$$ESF(x) = a\{1-\exp(-b\,|x-x_0|)\} + c\cdot erf(d^{1/2}\,|x-x_0|) \qquad (18)$$

$$MTF(f) = \frac{c\cdot\exp(-\pi^2 f^2/d) + a(1+4\pi^2 f^2/b^2)^{-1}}{(c+a)} \qquad (19)$$

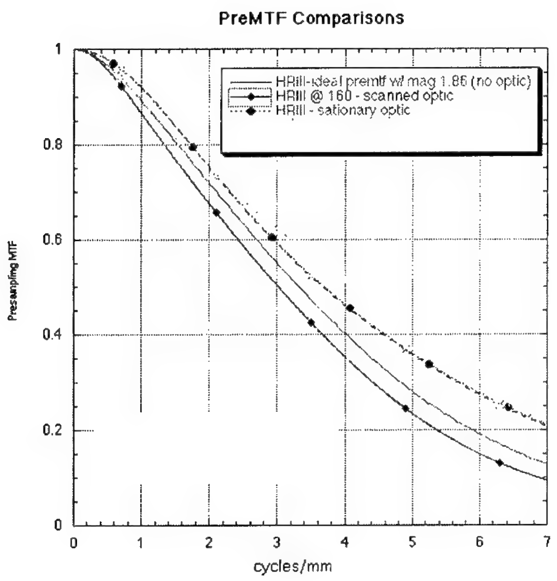

Figure 81 Calculated MTF compared with the MTFs with scan optics, and without optics.

The calculated MTF was compared with that from scanned optics in Figure 81 . The MTF from scanned optics was calculated from a slit image. Optic structure was smeared out with scanning, so no background deduction is necessary. An ideal MTF was also plotted in Figure 81 . An ideal MTF is the one when we assume the lens introduces only the 1.86 factor magnification and no image degradation. It is measured with a slit image without optics, and its result was multiplied by the magnification of the capillary lens. The measured MTF with lens should no better than the ideal MTF. However, for some reason, the MTF for stationary lens is better than the ideal MTF. It is possible that the background elimination process failed the MTF measurement. Another possibility is that the magnification of the lens is different from 1.86, since the magnification was measured separately at a different time.

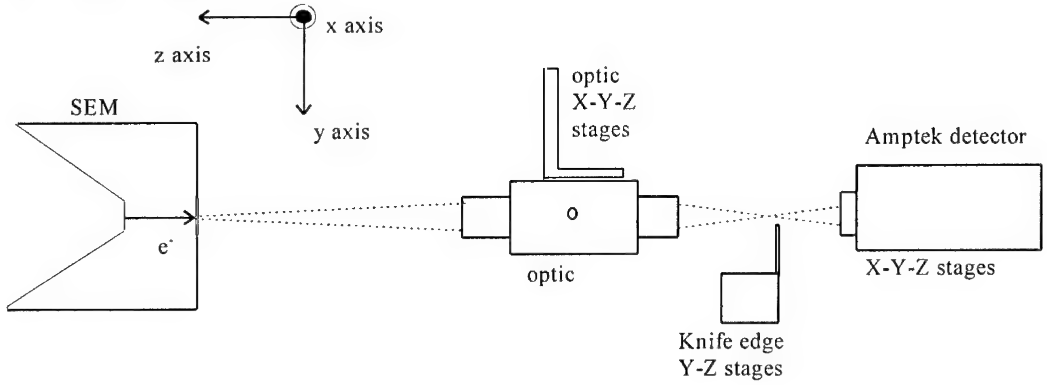

Figure 82. Schematic of the experimental setup for optic characterization.

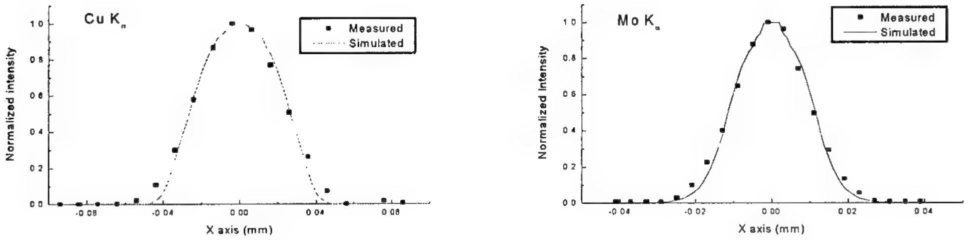

Figure 83. Focal spot scans of focusing optic.

6.3.1.5. DEMAGNIFYING, FOCUSING MONOLITHIC OPTICS

Monolithic optics similar to the collimating optic shown in can be used to minify an x-ray beam. Some characterization of such optics has been performed. The first measurement characterized an optic using a point source, a micro-focused transmission x-ray source (spot diameter about 5 μm) modified from an old SEM. Anode materials made of Cu and Mo are coated on a thin Be vacuum window. An energy-sensitive Amptek detector with an energy resolution of 250 eV at 5.9 keV was used for x-ray detection. The crystal size of the detector is 7 mm^2. The detector was placed roughly at the output focal plane of the optic, 8.5 mm away from the exit of the optic, to allow the detection of the output beam from the entire optic. The polycapillary focusing optic and detector were mounted on x-y-z stages which allows precise alignments among the source, optic, and detector. Figure 82 shows the schematic of the experimental setup. The alignment of the optic input focus to the source is achieved by moving the optic in all three orthogonal directions until the transmitted flux is maximized.

The measurement was performed by scanning a tungsten knife edge plate across the focused beam on the focal plane. The first derivative of the measured intensity as a function of the position of the knife edge gives the intensity distribution of the focused beam. This is shown in Figure 83,

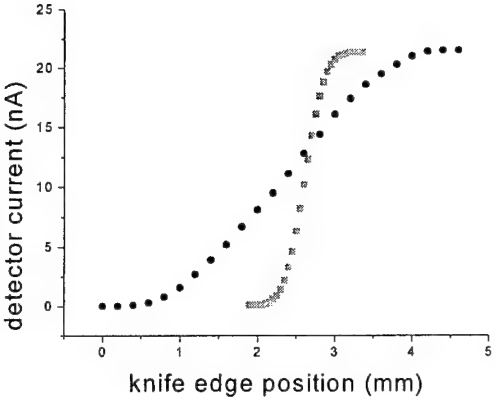

Figure 84. Knife edge scan at a knife edge to source scan distance of 103.5 (●) and 123.5 mm (▨).

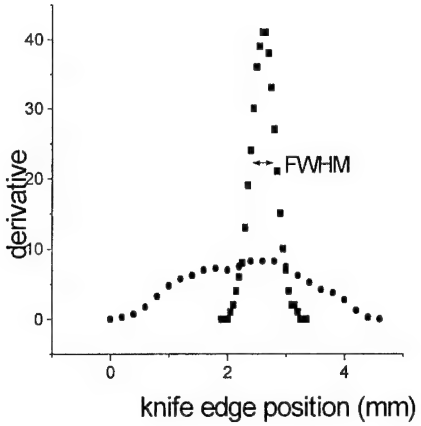

Figure 85. Derivative of knife edge scan for optic to knife edge distances of 103.5 mm (•) and 123.5 mm (■).

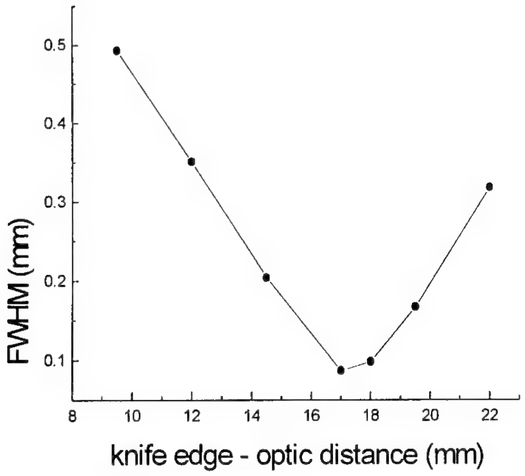

Figure 86. Width of derivative of knife-edge scan versus distance to optic for monolithic optic.

with the simulation results as comparisons. Good agreement between the measurements and the simulations indicate good alignment of the capillaries toward the output focus and that the simulation can reliably predict the divergence of the output beams from the capillaries. The measured spot sizes (FWHM) are 44 μm for Cu K_a and 21 μm for Mo K_a, respectively.

A second set of measurements were performed at beamline X23A3 at the National Synchrotron Light Source (NSLS) at Brookhaven National Laboratory (BNL). This is a white beam bending magnet line with a maximum white beam flux of approximately 13 W/cm^2. The size of the beam could be adjusted by two sets of collimating slits. The optic was mounted on a precision motion controlled four axis stage (up-down, left-right, tilt, and rotate). A knife edge or pinhole, mounted on another precision stage (left-right, forward-backward), could be placed between optic and the ion chamber. A small portable laser was used for rough alignment of the optics with the beam.

The spot size and also the focal distance were measured using a knife edge that was scanned horizontally across the beam. Two scans, one near to the focal spot of the multifiber optic and one 20 mm closer to the optic, are shown in Figure 84. The derivatives of these scans are shown in Figure 85. The scan close to the focal spot has a smaller width than the scan far away from the focal spot. A plot of the width of the scan derivative as a function of distance from the multifiber optic is given in Figure 86. Resulting calculated and measured gains are shown in table 4.

Table 4. Results for monolithic focusing optic.

X-Ray Energy (keV)	Spot size (mm)	Trans-mission (%)	measured Gain for 350 μm pinhole	calculated Gain 350 μm pinhole	calculated Gain 90 μm pinhole	calculated Gain 10 μm pinhole
6	0.09	36	78	81	645	911
8	0.08	49	96	110	933	1359
10	0.09	39	83	87	624	842
12	0.09	39	74	87	654	903
white	0.17	42	11	89	243	266

6.3.2. DIRECT DIGITAL DETECTORS

6.3.2.1. CZT DETECTOR

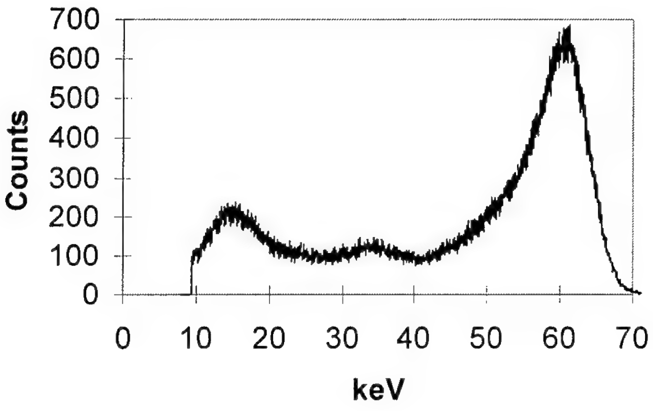

Figure 87. Spectrum from Am 241 taken with CZT single pixel detector.

Digirad, Inc. (formerly Aurora Technologies) was somewhat delayed by the late start date of their subcontract with the University at Albany due to contract formalities. However, a 1 cm long CZT array with 50 μm pixels has been manufactured and tested. The interconnect options were researched and the decision was reached to employ indium bump technology to bond the detector to a sapphire or quartz interconnect board, which is then bonded to the readout chips. This approach eliminates the need to wirebond to the detector, and also reduces the pixel size and consequently the leakage current. The first prototype was built, which demonstrated some mechanical instability. It is believed this is fixable with epoxy.

Measurements of room temperature energy bandwidth, detector quantum efficiency, and response uniformity were performed with a single pixel bulk CZT detector. Measurements of pixel to pixel variation using a scanned slit were performed with a linear CZT array.

6.3.2.1.1.1. Single pixel CZT detector

A single pixel detector 5.0 mm x 5.0 mm in area and 1.5 mm in thickness was used for the measurements. The external aluminum window was removed for the detector quantum efficiency measurement.

The spectrum produced by the CZT single pixel detector with a Am-241 radioactive source is shown in Figure 87. The spectrum was obtained with a Tennelec TC 241 linear preamplifier connected to a PCA-Multiport multichannel analyzer. The noise threshold at room temperature with this preamplifier is 10 keV. The FWHM of the Am 59.54 keV gamma is 9.5 keV at room temperature. The 17 and 24 keV lines of Am could not be resolved.

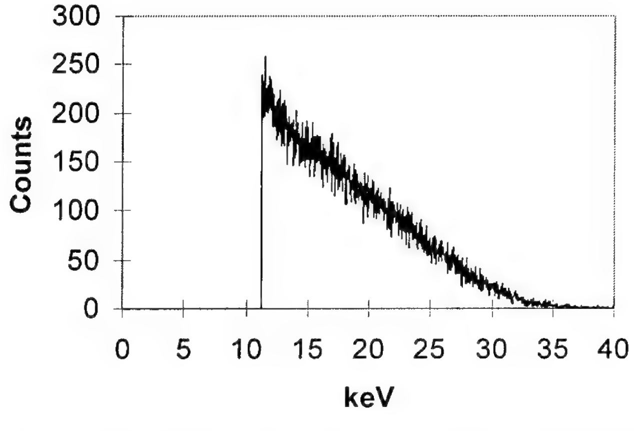

Figure 88. Spectrum of copper x-ray source, taken with single pixel CZT detector. The lower level discriminator was set at the lower end of the region of interest (ROI) marked in figure 5.

The detector quantum efficiency was measured in comparison to a high purity germanium (HpGe) detector with a 13 mm thick, 36 mm diameter crystal. For the HpGe detector, the efficiency was considered to be equal to unity in the energy range in which the experiment was performed. This detector was connected to the same linear amplifier and multichannel analyzer as the CZT detector. The distance between the source and the 100 μm pinhole was 50 cm.

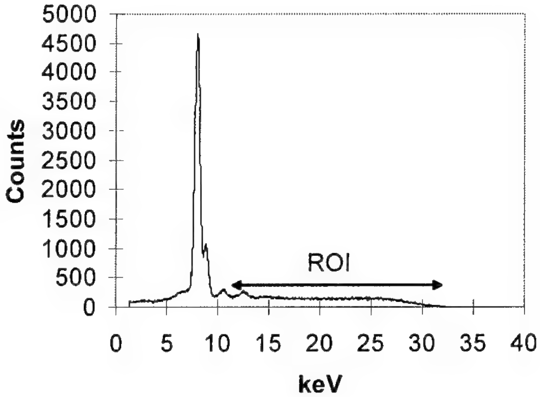

Figure 89. Spectrum of copper x-ray source, taken with HpGe detector. Lines at 10.5 and 12.6 keV are lead fluorescence from shielding. The region of interest (ROI) is marked.

The distance was chosen to maintain dead times less than 10%. The distance between the plane of the pinhole and the detectors was kept equal to 5 mm for both detectors, which was as small as possible given the HpGe detector geometry. The small separation reduces the effects of scattered or fluorescent radiation and ensures that the entire beam exiting the pinhole is intercepted by the detector. The HpGe detector was calibrated in energy using the Am gamma and the 5.9 keV line of Fe 55. The CZT detector was calibrated using the Am 59.54 keV line and a pulser set to equal and to half-height of this line.

Two different x-ray sources were used for this measurement. First was a copper x-ray tube with tube voltage of 30 kV, with the spectrum, obtained with the HpGe detector, shown in *Figure 89*. The resultant CZT spectrum for the same count time is shown in Figure 88. Interpretation of the results is complicated by two factors. First, the noise threshold, and therefore the lower level discriminator, is above the peak of the spectrum, so only the higher energy bremsstrahlung is recorded. Second, monoenergenic high energy photons, due to hole tailing effects, contribute to counts in a long Laurencian tail to lower energies, as seen for the Am gamma in Figure 87. Therefore counts due to photons with energy above the threshold are lost into lower energy channels. The detected quantum efficiency for this source, determined roughly as the ratio of integrated counts in the regions of interest shown in *Figure 89* and Figure 88, was found to be 44 %. A similar measurement was performed for a radioactive iodine source, with the spectra shown in

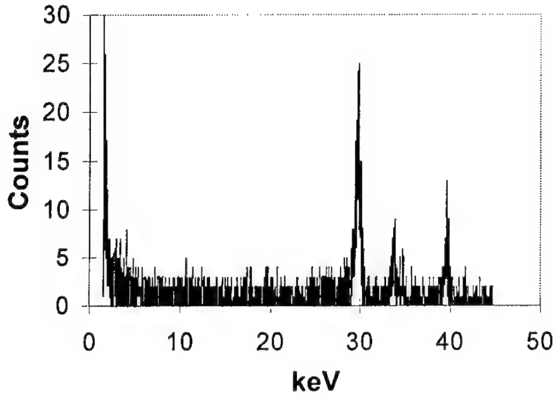

Figure 90. Spectrum from radioactive iodine taken with HpGe detector.

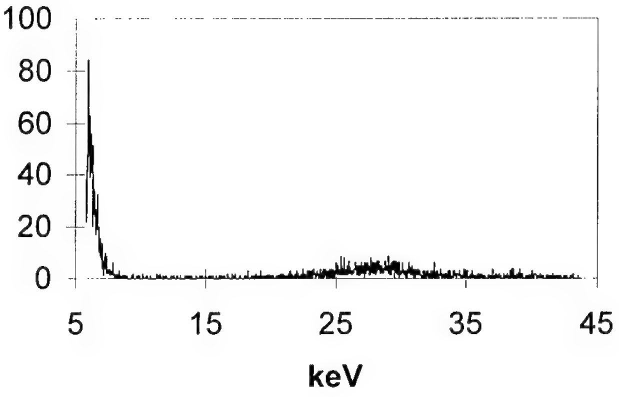

Figure 91. Spectrum from radioactive iodine taken with CZT detector

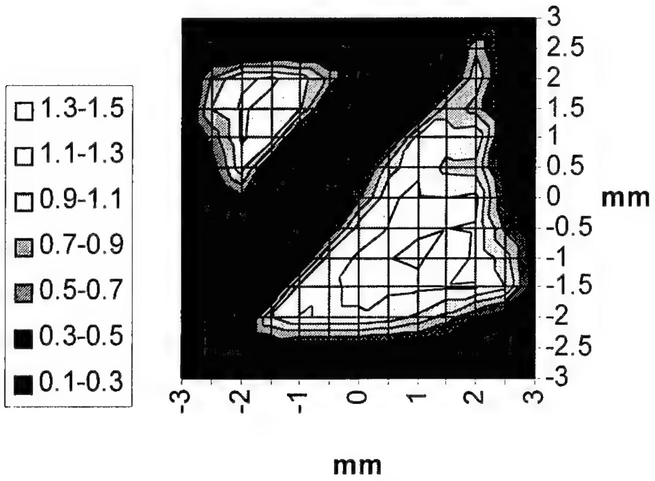

Figure 92. Pinhole scan of CZT single pixel with band of contact material.

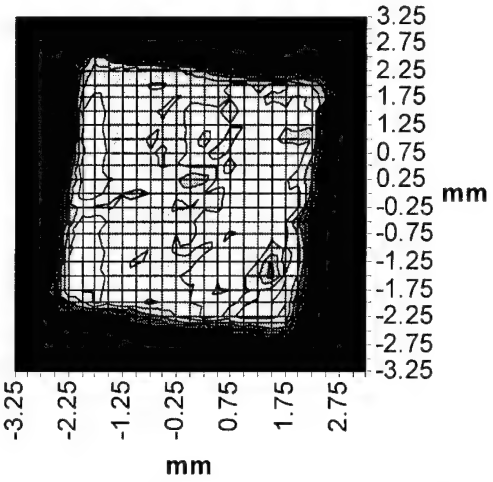

Figure 93. Pinhole scan of CZT single pixel.

Figure 91 and Figure 90. The DQE for this source is 42%. An imaging detector, which counts events independent of energy, would be affected by the hole-tailing only to the extent that the ends of the tail are below the noise threshold.

Area uniformity measurements were performed on a bulk single pixel detector by scanning the active area of the detector with a 300 μm pinhole. The result for the first detector tested is shown in *Figure 92*. The diagonal band is a strip of contact material normally unimportant for the operation of this detector in the infrared. The scan of a second detector, produced without this contact material, is shown in *Figure 93*. The average count rate in the 3.5 mm central area was normalized to unity. The variance in that region is 8%, 3% of which is due to Poisson statistics. Some part of the variance (4%) is due to the external aluminum window. The semiconductor sensitivity is quite uniform over the entire pixel.

6.3.2.1.1.2. Linear array

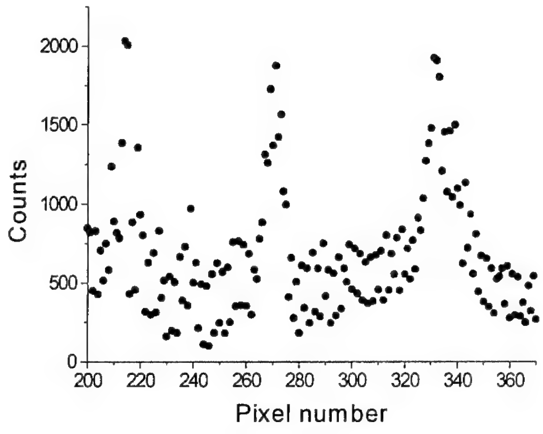

Figure 94. Image of slit taken with linear CZT array, without background subtraction.

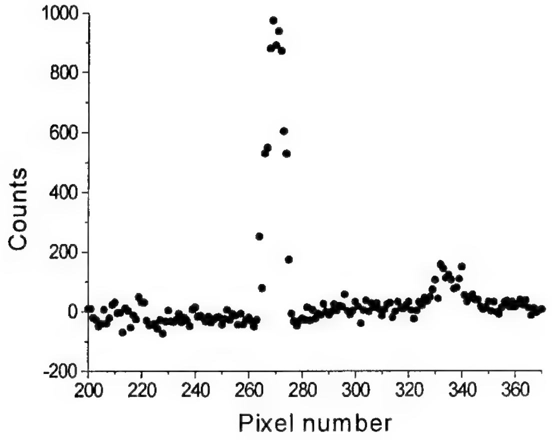

Figure 97. Slit image from Figure 94 with background from Figure 95 subtracted.

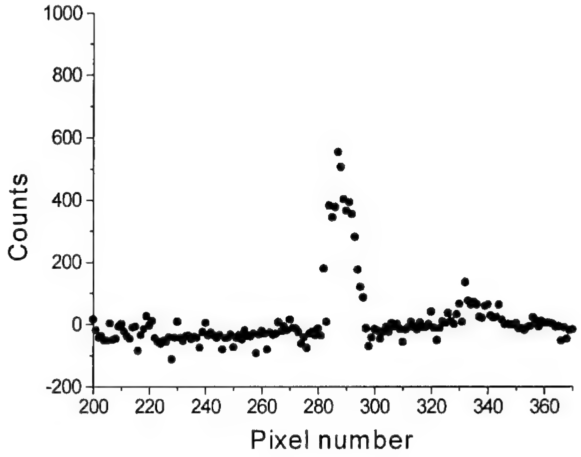

Figure 96. Background subtracted image of slit after moving detector to the left.

The CZT linear array was attached to the read-out electronics by means of indium bump bonding technology. Measurements were performed only for the central pixels because mechanical stresses caused bonding failure for the end pixels. This could be corrected for future arrays with an addition of epoxy for mechanical adhesion. To check the uniformity of the response of the pixels to x-ray radiation, a 0.5 mm slit was placed between the detector and the copper x-ray source. The array was then mounted on a translation stage that allowed movement parallel to the plane of the slit. The result without background subtraction is shown in Figure 94. The background, counted for the same period without the source on, is shown in Figure 95. The background subtracted result is shown in Figure 97. Moving the detector to the left causes the peak to move to the right, as shown in Figure 96. Comparing the peak heights of six positions along the central part of the array gives a peak height variance of 25%. To establish that the variance was due to differences in pixel sensitivity, a full field measurement was taken with no slit. Dividing the background subtracted slit image by the background subtracted full field image causes the two peak heights shown in Figure 97 and Figure 96 to agree within 6%.

Unfortunately, problems have developed in advancing this technology from linear to two dimensional arrays. Although only one-dimensional arrays were proposed in this project, it was recognized that the eventual outcome should be a 2D array. The current technology for 2D CZT arrays do not lend themselves to the small pixel sizes and relatively low x-ray energies (compared to nuclear gamma imaging) required for mammography.

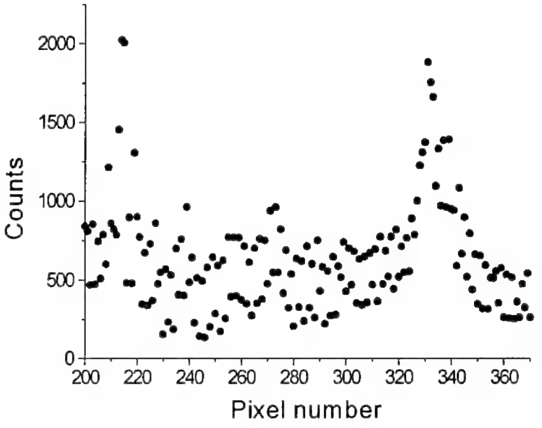

Figure 95. Background associated with image in Figure 94.

6.3.2.2. CID DETECTORS

Because of the questions in development of the CZT technology we have investigated a second technology, Charge Injection Devices (CID), as well. Like the more common CCD (Charge couple device) CID technology allows for rapid array imaging. Unlike the CCD, the CID is very radiation resistant. CID pixels can be read repeatedly and nondestructively, leading to very high dynamic range. CID well depths are also deeper than conventional CCDs, leading to a substantial reduction in blurring from high energy x-ray photons. The CID chips tested, which had 250x250 28 μm pixels, were too thin to have good x-ray quantum efficiency without phosphor. However, large area chip technology is already available. The measured DQE for the device was 23% at 20 keV. At that enery only 29% of the photons are expected to be absorbed in the 8 μm thick active region. Detector designs with thicker active areas will have larger DQEs. We then worked with the manufacturer, CIDTec, to study the application of their new x-ray dental imagers (with and without phosphor coatings) to mammography. Radiation damage testing measurements were completed on prototype imagers. Initial testing of a prototype imager with phospor resulted in mechanical stress damage which is being investigated. A second prototype for direct detection, without phosphor, has been delivered.

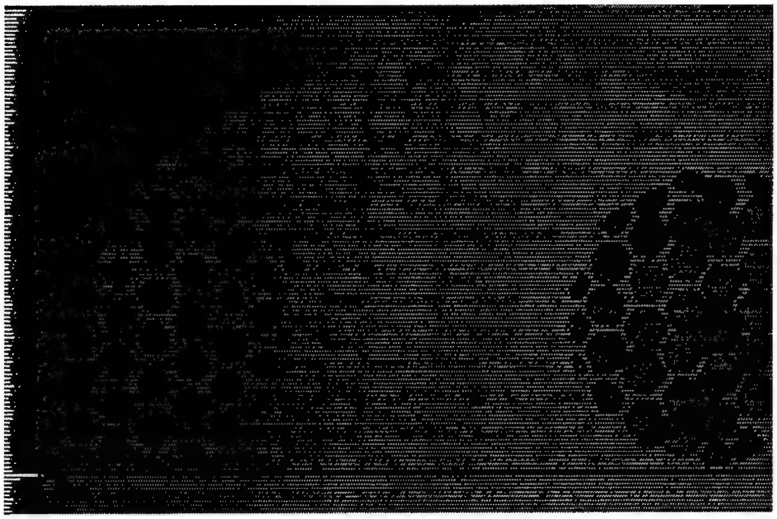

Figure 99. CID image of Lucite phantom shown in Figure 42.

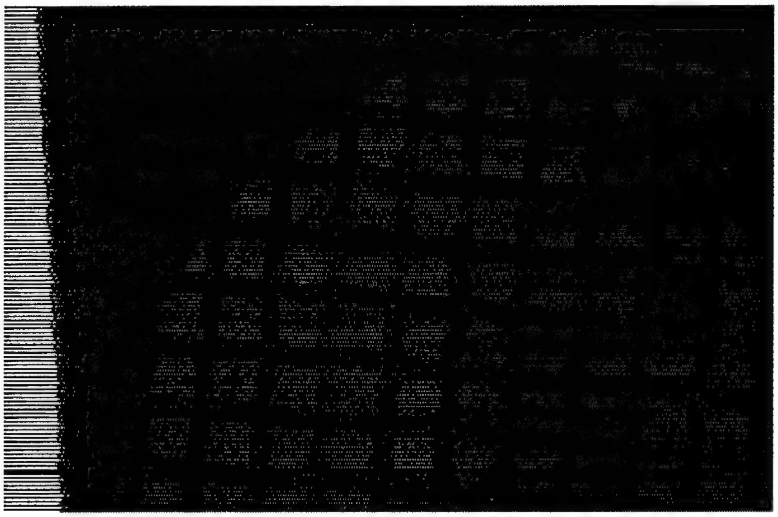

Figure 98. CID image of three grids. The largest has open spaces 560 microns wide and 300 micron wires. The smallest, unresolved at upper right, has 25 micron holes. The grid at center has 50 micron holes. The image was taken with magnification 1.02 onto the chip, which has 28 μm pixels.

7. Key Research Accomplishments

- Development of extensive modeling capability for polycapillary optics that includes realistic models for the effects of profile defects and shows extremely good agreement with measured data and therefore the capability to predict performance in new geometries.
- Measured polycapillary fiber transmission in excess of 65% at 20 keV for borosilicate glass and in excess of 50% for lead glass. Measured high angle transmission (which corresponds to scatter transmission) is lower than 1% for 12 cm long borosilicate glass optics and 1 cm long lead glass optics.
- Multifiber collimating optics technology has been developed. The newest optics have large capture angles and transmissions in excess of 30%, to efficiently redirect the divergent source into a parallel beam. The field uniformity is excellent. Such optics would provide gains of the order of 100x for monochromatic imaging.
- Modeling, measurement and defect studies have led to better manufacturing capabilities for magnifying tapered monolithic optics. These optics have demonstrated the ability to provide nearly ideal contrast enhancement, while at the same time increasing the system MTF performance at all spatial frequencies. A multitaper optic has been produced and tested.
- Image analysis studies have provided the means for image artifact analysis and reduction.
- Demagnifying optics, which could be used to reduce the size of the image onto a small pixel direct detector, have also been measured and perform well. The output spot sizes for these optics are as small as 20 μm.
- Two direct digital detectors have been extensively measured, CZT and CID technologies. These detectors provide signal directly from the x-ray photon, without using a phosphor for conversion to visible light, and so can provide inherently higher resolution. X-ray detection with two-dimensional array CID direct detectors has been demonstrated.

8. Reportable Outcomes

8.1. Manuscripts

Bradford CD, Peppler WW, Waidlich JM, Use of a slit camera for MTF measurements, accepted for publication in Medical Physics.

Lei Wang, C. A. MacDonald, and W. W. Peppler, “Performance of Polycapillary Optics for Hard X-ray Imaging,” accepted, Medical Physics.

Lei Wang, W.M. Gibson, C.A. MacDonald, “Potential of Polycapillary X-Ray Optics in Medical Imaging Applications,” in C.A. MacDonald, K.A. Goldberg, J.R. Maldonado, A.J. Marker III, S.P. Vernon, eds., **EUV, X-ray, and Neutron Optics and Sources**, SPIE vol. 3767, 1999.

S.D. Padiyar, M.V. Gubarev, Hui Wang, W.M. Gibson, C.A. MacDonald "Characterization of Polycapillary X-Ray Collimating Optics", in C.A. MacDonald, K.A. Goldberg, J.R. Maldonado, A.J. Marker III, S.P. Vernon, eds., **EUV, X-ray, and Neutron Optics and Sources**, SPIE vol. 3767, 1999.

S.M. Jorgensen, D.A. Reyes, C.A. MacDonald, E.L. Ritman, in U. Bonse, J.H. Dunsmuir, E.A. Hoffman, B.L. Illman, E.L. Ritman, "Micro-CT Scanner With A Focusing Polycapillary X-Ray Optic,"in **Developments in X-Ray Tomography II**, SPIE vol. 3772.

S.D. Padiyar, H. Wang, W.M. Gibson, C.A. MacDonald, M.V. Gubarev, "Beam Collimation Using Polycapillary X-Ray Optics For Large Area Diffraction Applications," in **Advances in X-ray Analysis**, 43, Proceedings of the 48th Denver X-ray Conference, 1999.

W.M. Gibson, C.A. MacDonald, J.B. Ulllrich, "Diffraction Geometry Optimization with Polycapillary X-Ray Optics", in C.A. MacDonald, K.A. Goldberg, J.R. Maldonado, A.J. Marker III, S.P. Vernon, eds., **EUV, X-ray, and Neutron Optics and Sources**, SPIE vol. 3767, 1999.

Hui Wang, Lei Wang, W.M. Gibson, C.A. MacDonald, "Simulation Study of Polycapillary X-Ray Optics," in **X-Ray Optics, Instruments, and Missions**, R.B. Hoover and A.B.C. Walker II, eds. SPIE Vol 3444, pp. 643-651, July 1998.

B.K. Rath, W.M. Gibson, Lei Wang, B.E. Homan and C.A. MacDonald, "Measurement and Analysis of Radiation Effects in Polycapillary X-ray Optics," Journal of Applied Physics, 83, no.12, pp. 7424-7435, June 15 1998.

C.C. Abreu and C.A. MacDonald, "Beam Collimation, Focusing, Filtering and Imaging with Polycapillary X-ray and Neutron Optics," invited review article, Physica Medica, vol. XIII, N.3, 1997, pp. 79-89.

C. Freinberg-Trufas, W.M. Gibson, S.M. Owens, C. H. Russell, C.A. MacDonald, F. P. Doty, "Measurements of a Prototype CdZnTe Array for Direct Digital Mammography," in **Hard X-ray and Gamma-ray Detector Physics Optics and Applications**, R.B. Hoover, F.P. Doty, eds., SPIE vol 3115, pp. 176-182, July 1997.

Lei Wang, B.K. Rath, W.M. Gibson, J.C. Kimball, C.A. MacDonald, "Performance Study of Polycapillary Optic Performance for Hard X rays," Journal of Applied Physics, **80** (7), pp.3628-3638, October 1, 1996.

D.G. Kruger, C.C. Abreu, E.G. Hendee, A. Kocharian, W.W. Peppler, C.A. Mistretta, C.A. MacDonald, "Imaging Characteristics of X-Ray Capillary Optics in Mammography," Medical Physics **23** (2), pp. 187-196, February 1996.

C.A. MacDonald, "Applications and Measurements of Polycapillary X-Ray Optics," Invited Paper, Journal of X-Ray Science and Technology, **6**, pp. 32-47, 1996.

Lei Wang, B.K. Rath W.M. Gibson, J.C. Kimball, and C.A. MacDonald, "Analysis of capillary optic performance for hard x rays", **Hard X-Ray/Gamma-Ray and Neutron Optics, Sensors, and Applications**, R.B. Hoover, and F.P. Doty, eds., SPIE Proceedings Vol. 2859, pp. 170-181, 1996.

R.G. Downing, W.M. Gibson, and C.A. MacDonald, "Polycapillary Optics: status, limitations and prospects", **Hard X-Ray/Gamma-Ray and Neutron Optics, Sensors, and Applications**, R.B. Hoover, and F.P. Doty, eds., SPIE Proceedings Vol. 2859, pp. 150-161, 1996.

C.A. MacDonald and W.M. Gibson, “Medical Applications of Polycapillary X-Ray Optics,” in **X-Ray and Ultraviolet Sensors and Applications**, R.B. Hoover and M.B. Williams, eds.,SPIE vol. 2519, pp. 186-196, July 1995.

Lei Wang and C.A. MacDonald, “Measurement of Capillary Optic Performance for Hard X rays,” in **X-Ray and Ultraviolet Sensors and Applications**, R.B. Hoover and M.B. Williams, eds., SPIE vol. 2519, pp. 218-223, July 1995.

B.K. Rath, D.C. Aloisi, D.H. Bilderback, N. Gao, W.M. Gibson, F.A. Hofmann, B.E. Homan, C.J. Jezewski, I.L. Klotzko, J.M. Mitchell, S.M. Owens, J.B. Ullrich, Lei Wang, G.M. Wells, Q.F. Xiao, and C.A. MacDonald, “Effects of intense x-ray radiation on polycapillary fiber performance,” in **X-Ray and Ultraviolet Sensors and Applications**, R.B. Hoover and M.B. Williams, eds., SPIE vol. 2519, pp. 207-217, July 1995.

C.C. Abreu, D.G. Kruger, C.A. MacDonald, C.A. Mistretta, W.W. Peppler, Q.F. Xiao, "Measurements of Capillary X-Ray Optics with Potential for Use in Mammographic Imaging," Medical Physics **22** (11), Pt. 1, pp. 1793-1801, November 1995.

B. Rath, R. Youngman, C.A. MacDonald, "An Automated Test System for Measuring Polycapillary X-Ray Optics," Review of Scientific Instrumentation, **65**, pp.3393-3398, Nov. 1994.

J.B. Ullrich, W.M. Gibson, M.V. Gubarev, C.A. MacDonald, "Potential for Concentration of Synchrotron Beams with Capillary Optics," Nuclear Instruments and Methods in Physics Research **A 347**, pp. 401-406, 1994.

P. Tompkins, C.C. Abreu, F. Carrol, Q. Xiao, C.A. MacDonald, "Use of Capillary Optics as a Beam Intensifier for a Compton X-Ray Source," Medical Physics, **21**, no. 11, pp. 1777-1784, 1994.

Kardiawarman, V. Kovantsev, S. Budkov, Q.F. Xiao, W.M. Gibson, C.A. MacDonald, P. Persans, L. Lurio, ‘Characterization of a Mult-Fiber Polycapillary-based X-Ray Collimating Lens,” in **X-Ray and UV Detectors**, SPIE vol. 2278, pp. 238-247, 1994.

R. Wentink, J. Carbone, D. Aloisi, W.M. Gibson, C.A. MacDonald, Q.E. Hanley, R.E. Fields, and M.B. Denton, “Charge Injection Detectors for X-Ray Imaging,” **in Advances**

in Multilayer and Grazing Incidence X-ray/EUV/FUV Optics, R.B. Hoover and A.B.C. Walker, Jr., eds., Proceedings of the SPIE vol. 2279, 1994, pp. 380-387.

W.M. Gibson and C.A. MacDonald, “Polycapillary Kumakhov Optics: A Status Report,” in **X-Ray and UV Detectors**, SPIE vol. 2278, pp. 156-167, 1994.

8.2. Presentations

C.A. MacDonald, "X-ray Optics for Scatter Rejection" Invited Talk, General Electric Corporate Research & Development, 6/99.

S.D. Padiyar, H. Wang, W.M. Gibson, C.A. MacDonald, M.V. Gubarev, “Beam Collimation Using Polycapillary X-Ray Optics For Large Area Diffraction Applications,” Denver X-ray Conference, 1999.

S.M. Jorgensen, D.A. Reyes, C.A. MacDonald, E.L. Ritman, “Micro-CT Scanner With A Focusing Polycapillary X-Ray Optic,” SPIE 1999.

Lei Wang, W.M. Gibson, C.A. MacDonald, “Potential of Polycapillary X-Ray Optics in Medical Imaging Applications,” SPIE vol. 1999.

S.D. Padiyar, M.V. Gubarev, Hui Wang, W.M. Gibson, C.A. MacDonald “Characterization of Polycapillary X-Ray Collimating Optics”, SPIE 1999.

Bradford CD, Peppler WW, “Use of a slit camera for MTF measurements”, RSNA, November 1998.

C.A. MacDonald, “Medical and biological applications of Polycapillary Optics” Invited Talk, Mayo Clinic, Rochester, Minn, 9/98.

C. Freinberg-Trufas, W.M. Gibson, S.M. Owens, C. H. Russell, C.A. MacDonald, F. P. Doty, “Measurements of a Prototype CdZnTe Array for Direct Digital Mammography,” SPIE, July 1997.

Lei Wang, B.K. Rath W.M. Gibson, J.C. Kimball, and C.A. MacDonald, "Analysis of capillary optic performance for hard x rays", SPIE 1996.

C.A. MacDonald, “Roughness effects, radiation damage and applications” Invited Talk, Capillary Developer’s Workshop, Cornell, 10/96.

R.G. Downing, W.M. Gibson, and C.A. MacDonald, "Polycapillary Optics: status, limitations and prospects", SPIE 1996.

C.A. MacDonald, “Radiography with Polycapillary Optics,” Invited Talk, NYS AAPM, 10/96.

C.A. MacDonald and W.M. Gibson, "Medical Applications of Polycapillary X-Ray Optics," SPIE July 1995.

Lei Wang and C.A. MacDonald, "Measurement of Capillary Optic Performance for Hard X rays," SPIE July 1995.

B.K. Rath, D.C. Aloisi, D.H. Bilderback, N. Gao, W.M. Gibson, F.A. Hofmann, B.E. Homan, C.J. Jezewski, I.L. Klotzko, J.M. Mitchell, S.M. Owens, J.B. Ullrich, Lei Wang, G.M. Wells, Q.F. Xiao, and C.A. MacDonald, "Effects of intense x-ray radiation on polycapillary fiber performance," SPIE July 1995.

C.A. MacDonald, "Medical Applications of Capillary Optics" Invited Talk, SPIE 7/95.

C.A. MacDonald, "Medical Applications of Capillary Optics" Invited Talk, NYS APS Sectional Meeting, 4/95.

Peppler WW, Kruger DG, Abreu CC, MacDonald CA, Kocharian A, Hendee E, "Digital Mammography with use of x-ray capillary optics", RSNA, November, 1995.

Kruger DG, Abreu CC, Peppler WW, MacDonald CA, Mistretta CA, "Imaging characteristics of x ray capillary optics in mammography", AAPM, July, 1994.

Kruger DG, Abreu CC, Peppler WW, MacDonald CA, Mistretta CA "X-ray capillary optics for improved resolution and contrast in digital mammography", RSNA, November, 1994.

C.A. MacDonald, "Capillary Optics for X Rays and Neutrons" Materials Research Society, Short Course Tutorial, 11/94

R. Wentink, J. Carbone, D. Aloisi, W.M. Gibson, C.A. MacDonald, Q.E. Hanley, R.E. Fields, and M.B. Denton, "Charge Injection Detectors for X-Ray Imaging," SPIE 1994.

W.M. Gibson and C.A. MacDonald, "Polycapillary Kumakhov Optics: A Status Report," SPIE 1994.

8.3. Poster Presentations

Hui Wang, Lei Wang, W.M. Gibson, C.A. MacDonald, "Simulation Study of Polycapillary X-ray Optics," SPIE San Diego 7/98.

C.A. MacDonald, C.C. Abreu, S. Padiyar, C. Freinberg-Trufas, Hui Wang, Lei Wang W.W. Peppler, E.G. Hendee, A. Kocharian, D.G. Kruger, F. P Doty, "Direct Digital Mammography Using Capillary Optics," DOA Breast Cancer Research Project Meeting 10/97.

8.4. Degrees Awarded

Hui Wang, "Analysis and Measurement of Polycapillary X-ray Collimating Lenses for Medical Imaging," Ph.D 1999, University at Albany.

Lei Wang, "Polycapillary Optics for Hard X Rays," Ph.D 1997, Distinguished Dissertation Award, University at Albany.

David Kruger, "Imaging Characteristics of X-ray Capillary Optics for Application to Digital Mammography," Ph.D., 1995, University of Wisconsin-Madison.

Bimal Rath, "Radiation Effects in Capillary X-Ray Optics," Ph.D 1995, University at Albany.

Kardiawarman, "Multifiber Polycapillary-Based X-Ray Collimating Lens for X-Ray Diffraction Experiments," Ph.D 1995, University at Albany.

Christorpher Jezewski, "The Characterization of a Multi-Fiber Polycapillary-based X-Ray Focusing Lens with 8 keV X Rays," MS, 1996, University at Albany.

David Aloisi, "The Charge Injection Device as a Position-Sensitive X-ray Detector," MS 1997, University at Albany.

8.5. Funding Generated

National Institutes of Health (NIH), subcontract to Univ. of Wisconsin (UW), "X-Ray Optical Mammography and Chest Radiography (Continuation)", Subcontract Principal Investigator, 11/1/97-12/31/00, Subcontract amount $423,741.

NIH, subcontract to UW, "Capillary Optics for Superior Mammographic Image Quality," Subcontract Principal Investigator, 4/98-3/01, Subcontract amount $373,845.

NYS Science and Technology Foundation, Center for Advanced Technology, 7/94-3/95, $83,005 matching funds.

NIH, subcontract to UW, "Capillary Optics for Mammography and Chest Radiography," Subcontract Principal Investigator, 1/93-6/96, Subcontract Amount, $298,785.

8.6. Funding Pending

NASA/XOS, High efficiency polycapillary optics for hard x-ray astrophysics, subcontract principal investigator, 9/99-8/02, $165,000.

NSF/Mayo Clinic, "Multidisciplinary micro CT 3D imaging facility," consultant, 9/99-9/04, $16,500

NASA/XOS, Low Power Convergent Beam MXRF/XRD System for Lander/Rover Applications, subcontract principal investigator, 1/1/2000-6/30/2000, $20,000.

NIH/XOS, "Improvement of Medical Imaging with Capillary Optics," subcontract principal investigator, 9/99-8/01, $118,697.

8.7. Employment/Research Received

8.7.1. RESEARCH AWARDS

Lei Wang, Breast Cancer Research Project Postdoctoral Fellowship, 1997
Hui Wang, Breast Cancer Research Project Predoctoral Fellowship, 1997
Sushil Padiyar, Breast Cancer Research Project Predoctoral Fellowship, 1997

8.7.2. RESEARCH EMPLOYMENT

Lei Wang, Postdoctoral Residency, University of California at San Francisco, 1999.

David Kruger, Mayo Clinic, 1995.

Bimal Rath, Wadsworth State Health Laboratory, 1995.

Christorpher Jezewski, X-ray Optical Systems, Inc., 1996.

David Aloisi, X-ray Optical Systems, Inc., 1997.

9. Conclusions

This is a high risk project with potentially very high gain. Any such project will have inevitable delays, frustrations and changes of direction. However, the delays and problems associated with this project have been fairly minor. Some manufacturing problems have occurred with both optics and detectors. These problems have been addressed by our studies of defect properties, and by changes being adopted in the manufacturing processes. Notwithstanding the problems, the optics tested have performed extremely well. A number of promising geometries are being studied: collimating optics with long and short focal lengths, with and without antiscatter optics, monolithic linear magnifying tapers, and monolithic focusing, demagnifying optics. The collimating optics have transmissions in excess of 30% at their design energies, with collection angles ranging from 8 to 12 degrees. Scatter rejection is very high from all the optics. The linear tapers resulted in nearly ideal contrast enhancements and simultaneously increase in MTF at all spatial frequencies. This will result in an improvement in resolution regardless the inherent spatial resolution of the detector. Just as important, if less spectacular, is the rapidly growing modeling capability. The modeling has lead to a real development of understanding of the nature of polycapillary defects, which is already leading to improvements in the manufacturing processes. Further, the increased confidence in the modeling allows future lens geometries to be effectively "tested" in simulation so that design parameters can be rapidly optimized.

Direct digital detector development is also promising. Two diverse detector technologies have been investigated. Both show considerable promise for providing simultaneous high resolution and high quantum efficiency. One dimensional "imaging" was demonstrated with the CZT linear array. The CZT detector has higher quantum efficiency without phosphor, but is more difficult to produce as a two-dimensional array with sufficiently low read-out noise and small enough pixels. However, this is largely a problem with the read-out electronics. As better electronics are becoming rapidly available, this technology becomes more attractive. The CID technology, while it would require some modification for phosphor free operation, is moving rapidly into the x-ray market, particularly in dental imaging. CID two dimensional array technology with small pixel sizes already exists. This is another promising new technology for mammography.

10. References

[1]Shern, F., Digital Mammography and Related Technologies: A Perspective from the national Cancer Institute, Radiology, 183(3), p.629-630, 1992.

[2] M.A. Kumakhov, F.F. Komarov, "Multiple Reflection from Surface X-ray Optics," Physics Reports, **191**, (5): p. 289-350, 1990.

[3] C.A. MacDonald, C.C. Abreu, S.S. Budkov, H. Chen, X. Fu, W.M. Gibson, Kardiawarman, A. Karnaukhov, V. Kovantsev, I. Ponomarev, B.K. Rath, J.B. Ullrich, M. Vartanian, Q.F. Xiao, "Quantitative Measurements of the Performance of Capillary X-ray Optics," Multilayer and Grazing Incidence X-ray/EUV Optics II, R.B. Hoover and A. Walker, eds., SPIE Proc. vol. 2011, 1993.

[4] J.B Ullrich, V. Kovantsev, C.A. MacDonald, "Measurements of Polycapillary X-ray Optics," Jour. Appl. Phys., **74** (10), Nov. 15, 1993.

[5] C.A. MacDonald, "Applications and Measurements of Polycapillary X-Ray Optics," Journal of X-Ray Science and Technology, **6**, pp. 32-47, 1996..

[6]C.C. Abreu, D.G. Kruger, C.A. MacDonald, C.A. Mistretta, W.W. Peppler, Q.F. Xiao, "Measurements of Capillary X-Ray Optics with Potential for Use in Mammographic Imaging," Medical Physics **22** (11), Pt. 1, pp. 1793-1801, November 1995.

[7]A. G. Haus, in **Screen Film Mammography**, G.T. Barnes and G. Donald Frey, eds., Medical Physics Publishing, Madison, Wisconsin, 1991.

[8]B.H. Hasegawa, The Physics of Medical X-ray Imaging, 2nd Ed., Medical Physics Publishing, Madison, Wisconsin, 1991.

[9]Q.F. Xiao, I.Y. Ponamarev, A.I. Kolomitsev and J.C. Kimball, in R.B. Hoover, ed., **X-ray Detector Physics and Applications**, SPIE 1992.

[10]B.L. Henke, E.M. Gullikson, and J.C. Davis, Atomic Data and Nuclear Data Tables, **54 (2), p. 181, 1993.**

[11]Lei Wang, B.K. Rath, W.M. Gibson, J.C. Kimball, C.A. MacDonald, "Measurement and Analysis of Capillary Optic Performance for Hard X rays,", Jour. Appl. Phys., September 15, 1996.

[12] Hui Wang, Lei Wang, W.M. Gibson, C.A. MacDonald, “Siumlation Study of Polycapillary X-Ray Optics,” in SPIE Vol 3444, July 1998.

[13]Lei Wang and C.A. MacDonald, "Measurement of Capillary Optic Performance for Hard X rays," in R.B. Hoover and M.B. Williams, **X-ray and Ultraviolet Sensors and Applications**, SPIE vol. 2519, July 1995.

[14]Lei Wang and C.A. MacDonald, "Measurement and analysis of capillary optic performance for hard x-rays", **Hard X-ray/Gamma-Ray and Neutron Optics, Sensors, and Applications**, R.B. Hoover, and F.P. Doty, eds., SPIE Proceedings Vol. 2859.

[15] Lei Wang, C. A. MacDonald, and W. W. Peppler, Performance of Polycapillary Optics for Hard X-ray Imaging, accepted, Medical Physics.

[16] B.K. Rath, W.M. Gibson, Lei Wang, B.E. Homan and C.A. MacDonald, "Measurement and Analysis of Radiation Effects in Polycapillary X-ray Optics," Journal of Applied Physics, 83, no.12, pp. 7424-7435, June 15 1998.

[17] B.K. Rath, D.C. Aloisi, D.H. Bilderback, N. Gao, W.M. Gibson, F.A. Hofmann, B.E. Homan, C.J. Jezewski, I.L. Klotzko, J.M. Mitchell, S.M. Owens, J.B. Ullrich, Lei Wang, G.M. Wells, Q.F. Xiao, and C.A. MacDonald, Effects of intense x-ray radiation on polycapillary fiber performance, in R.B. Hoover and M.B. Williams, **X-Ray and Ultraviolet Sensors and Applications**, SPIE vol. 2519, July 1995.

[18] C.C. Abreu and C.A. MacDonald, "Beam Collimation, Focusing, Filtering and Imaging with Polycapillary X-ray and Neutron Optics," invited review article, Physica Medica, vol. XIII, N.3, 1997, pp. 79-89.

[19] J.C. Kimball and D. Bittel, "Surface Roughness and Scattering of glancing angle x-rays: Applications to X-ray lenses" J. Appl. Phys, **74 (2),** 15 July 1993.

[20] S.D. Padiyar, M.V. Gubarev, Hui Wang, W.M. Gibson, C.A. MacDonald "Characterization of Polycapillary X-Ray Collimating Optics", in C.A. MacDonald, K.A. Goldberg, J.R. Maldonado, A.J. Marker III, S.P. Vernon, eds., **EUV, X-ray, and Neutron Optics and Sources**, SPIE vol. 3767, 1999.

[21] C. E. Dick and J. W. Motz, "New method for experimental evaluation of x-ray grids", Medical Physics, Vol. 5, No. 2, Mar./Apr. 1978.

[22] D.G. Kruger, C.C. Abreu, E.G. Hendee, A. Kocharian, W.W. Peppler, C.A. Mistretta, C.A. MacDonald, "Imaging Characteristics of X-Ray Capillary Optics in Mammography," Medical Physics **23** (2), pp. 187-196, February 1996.

[23] C.D. Bradford, W.W. Peppler, J.M. Waidelich, "Use of a Slit Camera for MTF Measurements," accepted, Medical Physics.

[24] Qin-sheng Chen, Michel Defrise, and F. Deconinck, "Symmetric Phase-Only Matched Filtering of Fourier-Mellin Transforms for Image Registration and Recognition", IEEE

Transactions on Patern Analysis and Machine Intelligence, Vol. 16, No. 12, December, pp. 1156.

[25] Hiroshi Fujita, et. al. "A Simple Method for Determining the Modulation Transfer Function in Digital Radiography", IEEE Transaction on Medical Imaging, Vol. 11, No. 1, pp. 34.

[26] Ehsan Samei, Michael J. Flynn, David A. Reimann, "A Method for Measureing the Presampled MTF of Digital Radiographic Systems using an Edge Test Device", manuscript submitted to Medical Physics, 1996.

[27] John M. Boone and Seibert, "An analytical edge spread function model for computer fitting and subsequent calculation of the LSF and MTF", Medical Physics, Vol. 21, No. 10. October 1994., pp.1541

11. Final Bibliography

11.1. PUBLICATIONS

see section 8.1, page 53.

11.2. MEETINGS

see section 8.2, page 56.

11.3. PERSONNEL

Walter W. Peppler
Carolyn A. MacDonald
Carla Bradford
David Kruger
Frank Hoffmann
Sushil Padiyar
Cari
Suparmi
Francisca Sugiro
Robin Moresi
Christi Freinburg-Trufas
Lee Britt
Brian Van de Worken
Hui Wang
Lei Wang
Bimal Rath
Barrie Homan
Mikhail Gubarev